



Cite this: *Nanoscale*, 2024, **16**, 5870

Received 4th December 2023,
Accepted 16th February 2024

DOI: 10.1039/d3nr06194a

rsc.li/nanoscale

Structure-driven tuning of catalytic properties of core–shell nanostructures

Ilya V. Chepkasov, * Aleksandra D. Radina and Alexander G. Kvashnin

The annual increase in demand for renewable energy is driving the development of catalysis-based technologies that generate, store and convert clean energy by splitting and forming chemical bonds. Thanks to efforts over the last two decades, great progress has been made in the use of core–shell nanostructures to improve the performance of metallic catalysts. The successful preparation and application of a large number of bimetallic core–shell nanocrystals demonstrates the wide range of possibilities they offer and suggests further advances in this field. Here, we have reviewed recent advances in the synthesis and study of core–shell nanostructures that are promising for catalysis. Particular attention has been paid to the structural tuning of the catalytic properties of core–shell nanostructures and to theoretical methods capable of describing their catalytic properties in order to efficiently search for new catalysts with desired properties. We have also identified the most promising areas of research in this field, in terms of experimental and theoretical studies, and in terms of promising materials to be studied.

Introduction

Metal nanoparticles have been a focus of research over the last few decades. Interest has been aroused because it has been observed that the transition from microparticles to nanoparticles leads to enormous changes in the physical and

Skolkovo Institute of Science and Technology, 121205, Bolshoi Blv. 30, Building 1, Moscow, Russia. E-mail: I.Chepkasov@skoltech.ru



Ilya V. Chepkasov

Ilya Chepkasov, Ph.D., is a Senior Researcher at the Project Center for Energy Transition and ESG, Skolkovo Institute of Science and Technology (Skoltech). In 2010 he received a classical education in physics (Katanov Khakass State University). In 2016 he received a Ph.D. in Condensed Matter Physics from the Altai State Technical University. In 2018–2019 and 2021 he became a visiting scientist at the

Helmholtz-Zentrum Dresden-Rossendorf (Germany). In 2020 he started working at the Skolkovo Institute of Science and Technology as a research scientist. Since 2023, Ilya has been working in the position of Senior Researcher in the Industry-Oriented Computational Discovery group. His area of expertise is computational materials science with a focus on molecular dynamics and ab initio methods. His scientific interests include electronic, structural and catalytic properties of nanomaterials.



Aleksandra D. Radina

Ms Aleksandra D. Radina received her M.Sc. from NUST “MISiS”, Moscow, Russia. She is currently is a Ph.D. student and researcher at the Skolkovo Institute of Science and Technology, Moscow, Russia. Her scientific interests are in the areas of computational materials science, phase transitions, materials doping, chemical reactions, and catalysis.

chemical properties of the material.^{1–15} One of the most important features at the nanoscale is the small size of the particles, which leads to an increase in the surface-to-volume ratio¹⁶ and thus to an entry into the scale where quantum effects dominate. These effects make metal nanoparticles highly applicable in catalysis, which includes the production of fuels and chemicals, as well as the conversion of solar energy into chemical energy.^{17–24}

Haruta *et al.*²⁵ first discovered the ability of gold nanoparticles to catalyze the oxidation of carbon monoxide at low temperatures in 1987. This discovery sparked great interest in gold nanocatalysts as it challenged the traditional view that gold had no catalytic activity. The discovered nanoparticles had a small size of less than 5 nm, which was important for the efficiency of heterogeneous catalysis on oxide substrates. In the early 1990s, multilayered nanoparticles known as core–shell nanoparticles were synthesized.^{26–28} Core–shell nanoparticles are highly functionalized materials, leading to modified properties.^{29–32} The material properties can be modified by changing either the constituent materials or the core–shell ratio.³³

One of the major challenges often faced by chemists working in the field of catalysis is to develop catalytic systems that are highly active, selective, reliable, inexpensive, and environmentally sustainable. This issue could be partially or completely solved by the development of catalytic systems based on core–shell nanoparticles. Compared with alloy-based catalysts, core–shell catalysts have specific lattice strains and ligand effects that tailor the geometric and electronic properties.^{34–36} The catalytic activity of such a catalyst depends



Alexander G. Kvashnin

Alexander Kvashnin was born in 1989 in Krasnoyarsk, Russia. He received a master's degree in applied mathematics and physics from the Moscow Institute of Physics and Technology in 2012 and became a Ph.D. student at the same university. He also worked as a visiting researcher at Rice University in the USA in 2011 and 2013. Since 2015 he has been working as a research scientist at the Skolkovo Institute of Science and Technology. In

2016, Alexander received his Ph.D. in Condensed Matter Physics from the National University of Science and Technology MISIS. In 2021, he successfully defended his habilitation (Doctor of Sciences) thesis and obtained the habilitation degree in condensed matter physics. Since 2023, Alexander has held the position of Full Professor at Skoltech and has led the Industry-Oriented Computational Discovery group. In 2023 Alexander was listed in top 2% of the world's most cited researchers according to a single year impact compiled by Elsevier.

on the synergistic interactions between the core and the shell.³⁷ There are three main effects that can determine the catalytic activity of core–shell materials:³⁸ (1) the ligand effect, which refers to the interaction between the core and the shell that occurs due to the proximity of the atoms and affects the charge transfer between the components by altering the band structure; (2) the ensemble effect, which is governed by the adsorption of the material on the surface caused by the presence of different groups of atoms; and (3) the geometric effects, which result from the distinct reactivity of the surface atoms due to three-dimensional structural constraints such as surface tension.^{39,40}

These three factors can interact to significantly affect the overall reactivity. This is particularly the case for lattice strains, which typically exhibit significant modulation of the electronic properties of the shell and the corresponding reactivity.^{35,40–45} Core–shell nanoparticles are also economically valuable in that the core of an inexpensive material can be coated with shells of a more expensive material, not only enhancing the material properties. For example, inexpensive and effective catalysts can be produced by depositing noble metal catalysts as a monolayer on a base metal core.^{46,47}

Synthesis of core–shell nanostructures

Bimetallic core–shell nanoparticles can be successfully prepared by either colloidal synthesis³⁰ or gas-phase condensation.^{48,49} Condensation allows flexible control over materials, particle size, and shell thickness. To design core–shell nanoparticles with desired properties, it is crucial to understand the mechanisms that govern the core–shell preferences when two materials are mixed. This includes determining whether a core–shell structure will form and, if so, which material will occupy the core and which will form the shell.⁵⁰

The categorization of core–shell nanocrystals into three subgroups is based on the thickness of the shell, which greatly influences their physicochemical properties. These subgroups are defined by a single atomic layer, 2–6 atomic layers, and more than 6 atomic layers.⁵¹

A subtype of core–shell nanocrystals is a nanocrystal core encapsulated by a single atomic layer. There are several methods for growing a monolayer of one metal on the surface of another in a controlled manner. These methods include: seed-mediated growth, where stoichiometric condensation can be used to deposit just one atomic layer of the shell metal on the seed; the formation of a sacrificial monolayer by underpotential deposition, followed by the replacement of this layer by another metal with a higher reduction potential by galvanic replacement; and the formation of an alloy or intermetallic nanocrystal, followed by the induction of phase segregation. For most bimetallic combinations a single atomic layer shell structure is a non-equilibrium configuration. Interdiffusion can occur with prolonged exposure to high temperatures.

Core–shell nanoparticles have a shell range of 2–6 atomic layers, which is the characteristic thickness that allows strain

and electronic coupling between the core and shell. Four general methods exist for the controlled generation of nanocrystals: seed-mediated growth, sequential underpotential deposition and galvanic replacement processes, phase segregation, and anion coordination. Seed-mediated growth involves controlling the salt precursor to seed ratio to grow the shell to a desired thickness. Sequential underpotential deposition and galvanic replacement processes are repeated to achieve the desired result. Phase segregation, common to the Pt–Ni system, involves the concentration of Pt atoms at the surface, forming an ultrathin Pt skin.⁵² Anion coordination involves seeds stabilized with ligands containing functionalities capable of binding the metal precursor prior to reduction. It is important to note that these methods are objective and do not involve subjective evaluations unless clearly labelled as such.⁵³

For core–shell nanoparticles with shells thicker than six atomic layers, the electronic coupling between the core and the outermost layer in the shell is lost. As a result, the ability to access the strain-dependent catalytic activity is also lost. However, there are several advantages to core–shell nanocrystals with thick shells. These include the ability to tune optical properties over a wide range, enhance thermal and chemical stability, and in some cases, enhance magnetic properties. The most commonly used methods for controlled deposition of thick shells are based on seed-mediated growth. In this process, a metal-containing precursor is reduced or thermally decomposed in the presence of preformed seeds.

Structure-driven tuning of catalytic properties

Core–shell nanoparticles

One way to improve catalytic activity is to tune the lattice strain.^{17,34,35,39–41,43,54} Previous studies have mainly focused on modifying the composition and structure of the metal core to control the lattice strain.^{39,40,43,54–56} However, particle size plays an important role in bimetallic catalysts. In particular, as the size of the core decreases, the metallic core undergoes significant lattice shrinkage and changes in electronic properties such as work functions.^{57–61} These changes can have a significant impact on the lattice strain and charge transfer within the shell,⁶² thereby affecting the bimetallic synergy. Tuning the size of the core can solve the lattice deformation issue and improve the reactivity of the shell.

Recently Zhang *et al.*⁶³ investigated the strain and ligand effects of core–shell nanoparticles in the oxidation of benzyl alcohol (BzOH) to benzyl aldehyde. To disentangle the strain and ligand effects modulated by the core size and shell thickness, the authors first studied the adsorption of BzOH on different Au@Pd catalysts using density functional theory (DFT) calculations. Au₁₃@Pd₄₂, Au₅₅@Pd₉₂, Au₁₄₇@Pd₁₆₂, and Au₃₀₉@Pd₂₅₂ nanoparticles were used to study the adsorption of BzOH. The optimized Pd–Pd distance (on average) was found to be 2.72 Å for the small Au₁₃@Pd₄₂ cluster, gradually

increasing to 2.78 Å for the large Au₃₀₉@Pd₂₅₂ cluster, which is close to that in pristine Pd(111) (2.79 Å). Importantly, the adsorption of BzOH was studied at the same site for all nanoparticles. For Au₁₃@Pd₄₂ the adsorption energy of BzOH was −2.59 eV, and increasing the size of the nanoparticle to Au₅₅@Pd₉₂ leads to an increase in the adsorption energy to −2.88 eV (Fig. 1a). When the size is further increased to Au₁₄₇@Pd₁₆₂ and Au₃₀₉@Pd₂₅₂, the adsorption energy changes insignificantly (−2.96 and −2.90 eV respectively). The increase in adsorption with increasing cluster size can be explained by the reduction in lattice contraction, which is well described in ref. 35, 39 and 54. To model the adsorption of BzOH on large AuNP@Pd_{1ML} (at least 6.8 nm), where the lattice contraction in the Au core is completely reduced, an intact four-layer Au(111) surface with a 1 ML Pd overlayer, denoted Au(111)@Pd_{1ML}, was constructed. Although the Pd–Pd distance in the corresponding Pd layer is about 5% larger than that of Au₃₀₉@Pd₂₅₂, the calculated adsorption energy is −2.87 eV, which is 0.03 eV weaker than that of the nanoparticle. The slight weakening is explained by the fact that the gain in adsorption energy due to lattice stretching is compensated by the higher coordination number on the planar terrace (111) than on Au₃₀₉@Pd₂₅₂.

As mentioned above, in addition to lattice strain, ligand effects also play an important role in BzOH adsorption. Zhang *et al.*⁶³ found that for Au(111)@Pd_{1ML}, the subsurface metal directly under the topmost Pd layer is Au, which actually destabilizes the overall adsorption on BzOH. To clearly verify this, the Au substrate under Au(111)@Pd_{1ML} was removed and the corresponding BzOH adsorption energy was calculated without structural optimization (blue curve in Fig. 1a). The adsorption of BzOH on Pd_{1ML} without Au substrate becomes much stronger (−3.80 eV), and otherwise weakens to −2.87 eV. As in the case of Au(111)@Pd_{1ML}, the Au core in AuNP@Pd_{1ML} also destabilizes the adsorption of BzOH on Pd_{1ML}. As the cluster size decreases, the degree of destabilization caused by the Au substrate becomes smaller for small Au₁₃@Pd₄₂, Au₅₅@Pd₉₂, and Au₁₄₇@Pd₁₆₂ clusters. The variation in the destabilization of BzOH adsorption on the small AuNP@Pd_{1ML} clusters is attributed to the different lattice contractions.

Zhang *et al.*⁶³ showed that the ligand effects on the Au substrate side are localized only at the Au–Pd interface, and the destabilization decreases as the Pd thickness increases from 1 to 2 ML. The subsurface metal just below the top Pd layer is Pd rather than Au. The adsorption energy is highest at −3.34 eV for Au(111)@Pd_{2ML}. The adsorption of BzOH shows a pronounced quantum effect depending on the thickness of the Pd. It gradually weakens with a further increase in Pd thickness, and a very small change in adsorption energy (about −2.86 eV) is observed for $n \geq 4$ (n -number of layers). When the Pd thickness is increased from 2 to 6 ML, the surface Pd ε_{4d} shifts down from −1.64 to −1.74 eV with respect to the Fermi level, and similarly the subsurface Pd ε_{4d} shifts from −2.01 to −2.25 eV. These shifts reduce the corresponding reactivity and weaken the adsorption of molecules.

The obtained effects were then confirmed experimentally⁶³ by synthesizing a large set of Au@Pd core–shell nanoparticles

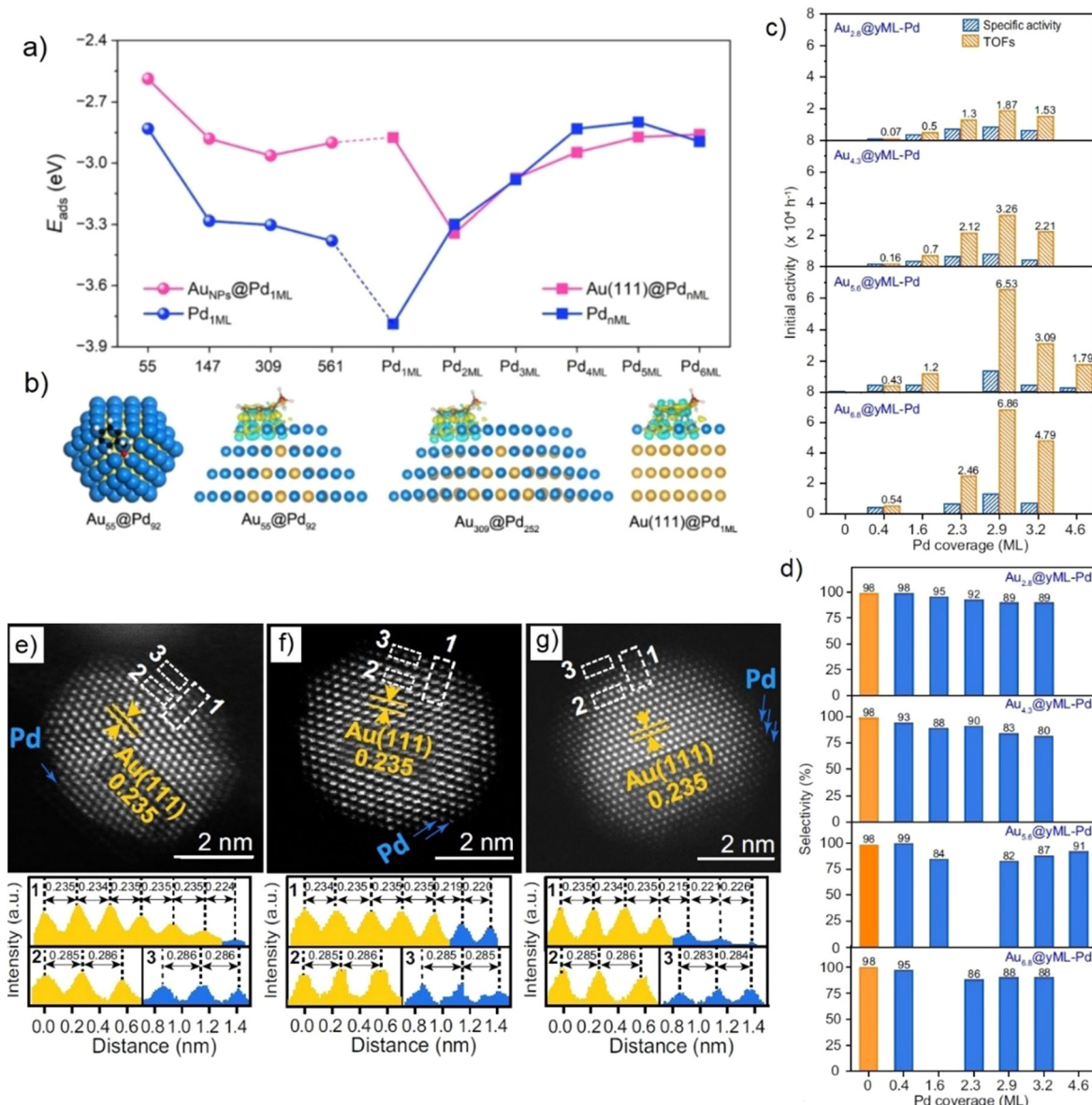


Fig. 1 (a) The adsorption energies of BzOH on $\text{Au}_{\text{NP}}@ \text{Pd}_{1\text{ML}}$ (pink circles) and $\text{Au}(111)@ \text{PdnML}$ (pink squares), and the blue counterparts representing the results without the presence of the Au core inside (for $\text{Au}_{\text{NP}}@ \text{Pd}_{1\text{ML}}$ clusters) or the Au substrate underneath (for $\text{Au}(111)@ \text{PdnML}$ slabs). (b) Top views of BzOH adsorption on $\text{Au}_{55}@\text{Pd}_{92}$ (blue = Pd, gold = Au, black = C, white = H, red = O) and the charge density difference contours for BzOH adsorption on $\text{Au}_{55}@\text{Pd}_{92}$, $\text{Au}_{309}@\text{Pd}_{252}$, and $\text{Au}(111)@\text{Pd}_{1\text{ML}}$. The navy blue and yellow contour areas represent the deficiency and excess of electrons respectively. (c and d) Specific activity and TOFs (c) and benzaldehyde selectivity (d) of the $\text{Au}_x@\text{yML-Pd}$ core–shell catalysts with an x nm Au monometallic layer. (e–g) Representative atomic-resolution HAADF-STEM images of $\text{Au}_{6.8}@\text{1.1ML-Pd}$ (e), $\text{Au}_{6.8}@\text{2ML-Pd}$ (f), and $\text{Au}_{6.8}@\text{2.9ML-Pd}$. Reproduced from ref. 63 with permission from Springer Nature, copyright 2023.

with precise adjustment of the Au core size from 2.8 to 6.8 nm and the Pd shell thickness from about 0.3 to 3.2 MLs (Fig. 1e–g). It was shown that in the solvent-free BzOH oxidation reaction, the trend of total activity as a function of Au size and Pd thickness is in perfect agreement with the calculated trend. A record high activity of $6.86 \times 10^4 \text{ h}^{-1}$ was obtained for an Au core size of 6.8 nm and a Pd shell thickness of ~2–3 ML (Fig. 1c and d). These results provide insight into the important role of the dual particle size effect in bimetallic catalysis, paving the way for the improvement of bimetallic catalysts.

As discussed above, the particle size determines the geometric and electronic structure of metallic nanoparticles, which shapes their catalytic activity. However, the size-dependent entanglement of geometric and electronic structures often leads to a trade-off between activity and selectivity, limiting the optimization of the overall catalytic performance. Bimetallic catalysts, whose unique strain and ligand effects provide another dimension to tune the geometric and electronic features,^{65,66} could overcome the entanglement effect that occurs when particle size is changed and resolve the activity–selectivity trade-off.

Guan *et al.*⁶⁴ investigated the enhancement of activity and selectivity of Au@Pt core–shell nanoparticles. First, the authors used DFT to study how the lattice parameters and electronic properties of the Pt monolayer on Au (1ML-Pt/Au(111)) substrate change. Fig. 2a clearly shows that the underlying gold expands the lattice of the supported platinum layer by 4.3% from 2.77 Å to 2.89 Å. This lattice expansion and the orbital hybridization between platinum and gold induce a significant upshift of the platinum 5d-band center by 0.69 eV towards the Fermi level (Fig. 2b). A shifted d-band center would make the exposed platinum layer more reactive. Based on the results of the theoretical calculations, the authors decided to experimentally study this effect on core–shell Au@Pt nanoparticles with different platinum shell thicknesses of Au@0.5ML-Pt, Au@1ML-Pt, and Au@2ML-Pt (Fig. 3). In the case of the Au@1ML-Pt nanoparticles, the platinum layer spacing within the platinum layer was ~2.86 Å, close to the underlying gold lattice, which was extended by 3.2% compared with bulk platinum (2.77 Å), in agreement with theoretical calculations (Fig. 3).

The catalytic activity of Au@Pt nanoparticles was investigated for the selective hydrogenation reaction of *para*-chloronitrobenzene (*p*-CNB).⁶⁴ In the chemoselective hydrogenation of *p*-CNB, the Au@0.5ML-Pt catalyst exhibited a selectivity of 99%, and the specific activity based on the platinum content was $1.75 \times 10^4 \text{ mol}_{\text{p-CNB}} \text{ mol}_{\text{Pt}} \text{ h}^{-1}$, higher than that of the most active sample of 2.7 nm-Pt (Fig. 4a). Au@1ML-Pt showed an even higher specific activity of $3.44 \times 10^4 \text{ mol}_{\text{p-CNB}} \text{ mol}_{\text{Pt}} \text{ h}^{-1}$ with high *p*-CAN selectivity (99%). Calculations of *p*-CAN formation rates showed that Au@1ML-Pt had the highest formation rate of $3.41 \times 10^4 \text{ mol}_{\text{p-CAN}} \text{ mol}_{\text{Pt}} \text{ h}^{-1}$, together with

99% selectivity and good recyclability (Fig. 4b). Thus Guan *et al.*⁶⁴ showed that a high activity and selectivity of core–shell catalysts can be achieved by fine-tuning the nanoparticle structure.

Bimetallic core–shell nanoparticles can also be effectively used in electrocatalysis, namely for energy conversion in fuel cells. Wang *et al.*³⁷ demonstrated a new low-cost catalyst for the oxygen reduction reaction (ORR) based on Pd@Pt_{nL} core–shell icosahedra nanoparticles with a well-controlled shell thickness. It is known that the specific activity of Pt(111) for the ORR is at least twice that of Pt(100).⁶⁷ Furthermore, the addition of surface strain can significantly modify the binding properties of adsorbates, which in turn affects their chemical reactivity.⁶⁸ The introduction of a compressive strain on the Pt lattice weakens the binding of adsorbed O and OH, thereby improving the ORR specific activity of Pt(111).⁶⁹ It has been found that the optimum compression is between 2 and 3%.^{70,71} Wu *et al.*⁷² found that the specific activity of Pt₃Ni icosahedra, with a tensile-stressed surface, was 1.5 times higher than that of Pt₃Ni octahedra of similar size, despite both having a surface covered by {111} facets. Thus, the use of nanocrystals with both {111} facets and twin defects on their surfaces can further enhance the specific activity of an ORR catalyst. Based on this observation, Wang *et al.*³⁷ explored the use of icosahedral Pd@Pt_{nL} (where the number of Pt layers, *n* = 0.7–4.3) to improve the Pt-based catalyst for the ORR, see Fig. 5a–f. This difference in the shell structure resulted in different catalyst activities.

The ORR activities of Pd@Pt_{nL} icosahedral nanoparticles (*n* = 0.7, 2.0, 2.7 and 4.3) were measured by their deposition on carbon. In the potential range of 0.86–0.94 V, the specific and mass activities of all Pd@Pt_{nL}/C catalysts were significantly improved compared with commercial Pt/C. In addition, the *j_k*-specific and *j_{k,mass}* of the Pd@Pt_{nL}/C catalysts showed a volcano-type dependence on the number of Pt atomic layers, with the Pd@Pt_{2.7L}/C catalyst exhibiting the highest specific and mass activities, as shown in Fig. 5g and h. At 0.9 V, the *j_k*-specific of Pd@Pt_{2.7L}/C catalyst was $1.36 \text{ mA cm}^{-2} \text{ Pt}$, which was 7.8 times higher than that of Pt/C ($0.174 \text{ mA cm}^{-2} \text{ Pt}$). The *j_{k,mass}* of Pd@Pt_{2.7L}/C ($0.64 \text{ A mg}^{-1} \text{ Pt}$) was 7.2 times higher than that of the Pt/C catalyst ($0.089 \text{ A mg}^{-1} \text{ Pt}$), making it a more critical indicator of the commercialization potential of the Pt-based catalyst.

The greatest increase in activity was found for the Pd@Pt_{2.7L}/C catalyst, which can be explained by a combination of both the core–shell structure and the compressive strain imposed on the Pt layers. Additional Pt atoms lead to a weakening of the binding strength of the reaction intermediates. To confirm this hypothesis, Wang *et al.*³⁷ performed a series of DFT calculations. The binding energies of OH on the Pt_{nL}^{*}/Pd(111)_{ico} were calculated and compared with the octahedral Pd@Pt_{3L} model surface.³⁷ The calculations showed that OH has a weaker binding affinity to the surface of Pt_{3L}^{*}/Pd(111)_{ico} than to the surface of Pt_{3L}^{*}/Pd(111)_{oct}, as long as the tensile strain in the (111) facet of a Pd icosahedron is 3% or lower than that of a Pd octahedron. The higher specific activity of

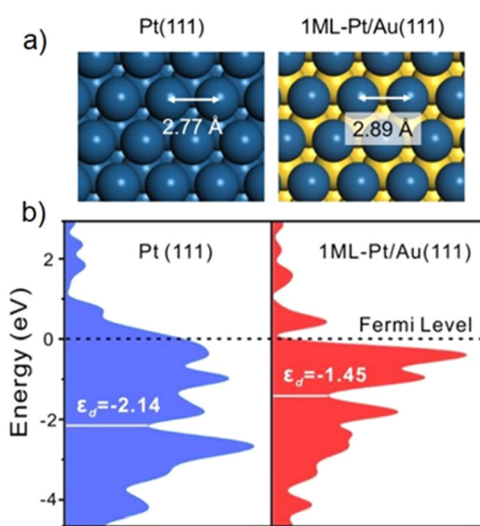


Fig. 2 (a) Lattice expansion of the Pt monolayer in 1ML-Pt/Au(111) compared with Pt(111). The navy and yellow spheres represent Pt and Au atoms respectively. (b) Density of states of the 1ML-Pt/Au(111) and Pt(111) surfaces. White horizontal lines show the energy of the d-orbitals of surface Pt atoms on Pt(111) and 1ML-Pt/Au(111) surfaces. Reproduced from ref. 64 with permission from Springer Nature, copyright 2021.

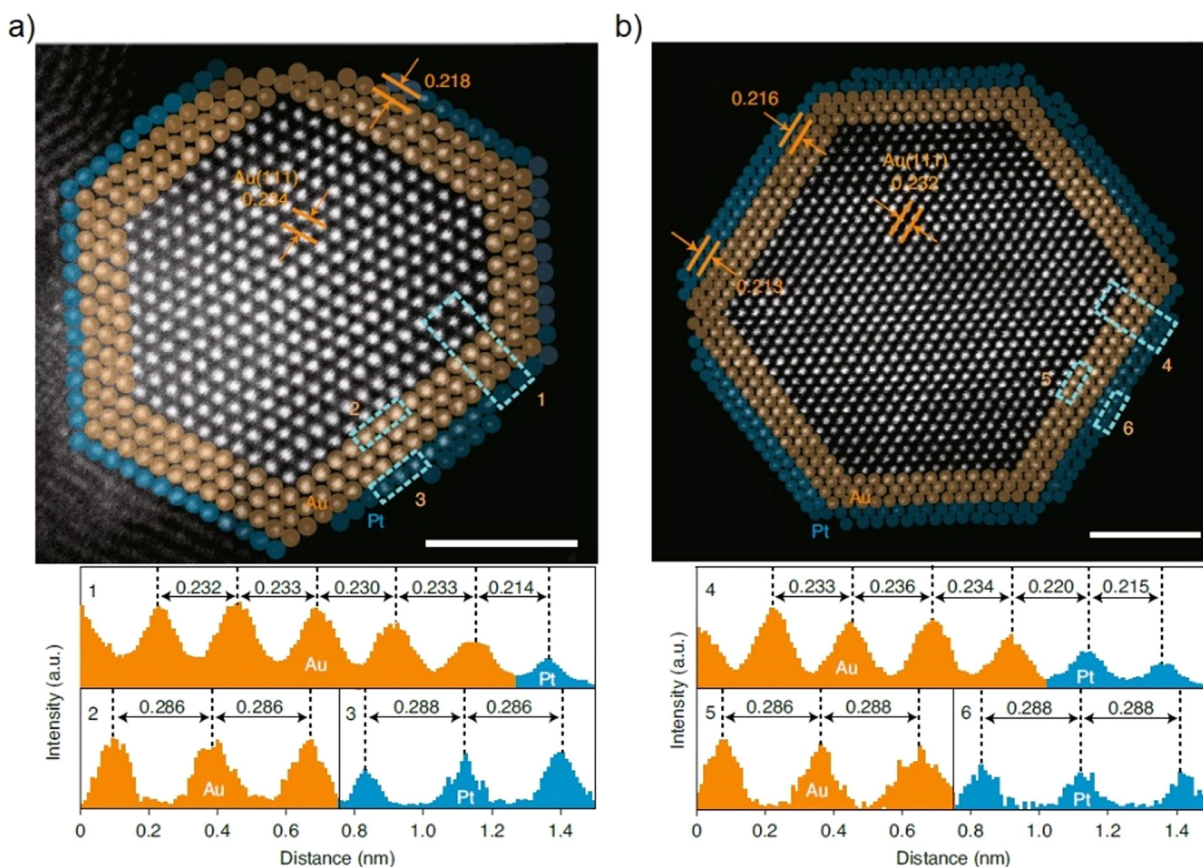


Fig. 3 Representative atomic resolution HAADF-STEM images of (a) Au@1ML-Pt and (b) Au@2MLPt catalysts, with the corresponding line intensity profiles along the numbered dashed rectangles to show the interplanar and lattice distances. In (a) and (b), the atoms in the outer layers are shown as light yellow and blue spheres to highlight the gold core and platinum shell. Reproduced from ref. 64 with permission from Springer Nature, copyright 2021.

the Pd@Pt_{3L} icosahedron compared with its octahedral counterpart results from weakened OH binding caused by a compressive strain in the Pt overlayers. By applying a simple electrochemical model, the experimentally observed relationship between the ORR specific activity and the number of Pt overlayers can be explained. In particular, they found a qualitative agreement between the theoretically predicted values and the experimentally obtained data (Fig. 5i), when the tensile strain in the Pd layers of the Pt_{nL}^{*}/Pd(111)_{ico} model was in the range of 2.4–3.0%.

For core-shell nanoparticles, the structure of the whole particle may also influence the catalytic activity. In particular, Chepkasov *et al.*⁷³ studied the correlation between the adsorption energy of O and CO and the structure (fcc, Ih, amorphous) of nanoparticles. The atomic structure of Au–Cu bimetallic alloy nanoparticles was obtained using MD modelling of the condensation process from the gas phase. Pure metal nanoparticles and core-shell nanoparticles were prepared by atomic substitution. To further investigate the influence of the composition and structure of Cu–Au nanoclusters on their reactivity, computational studies of the adsorption energies of CO and O on fcc, icosahedral and amorphous clusters with different

chemical distributions and compositions were carried out (Fig. 6).

The results indicate that the O binding energies in Cu–Au bimetallic alloy clusters are comparable to those calculated for pure Cu or core-shell Au@Cu nanoclusters. However, the distribution of binding energies is much broader in the former clusters. Clusters composed of pure Au and those with a Cu core and Au shell bind O atoms much less effectively than Cu–Au clusters. The structural characteristics of the clusters strongly influence the O binding energies in both pure Au clusters and core-shell Cu–Au clusters. Therefore, the average binding energies of O atoms in clusters with an fcc structure of pure Au or those with a Cu@Au core–shell structure are 0.38 and 0.59 eV more exothermic compared to corresponding cluster with an amorphous structure. Thus, the calculated O binding energies on a pure Au cluster with an fcc structure are only slightly less endothermic than those on the same cluster with an Au-core–Cu-shell structure, regardless of the completely different composition of the adsorption sites.

Although O atoms bind with comparable intensity to Cu–Au clusters with the Cu-core–Au-shell structure, the binding is significantly stronger with a pure Au composition using amorphous clusters.

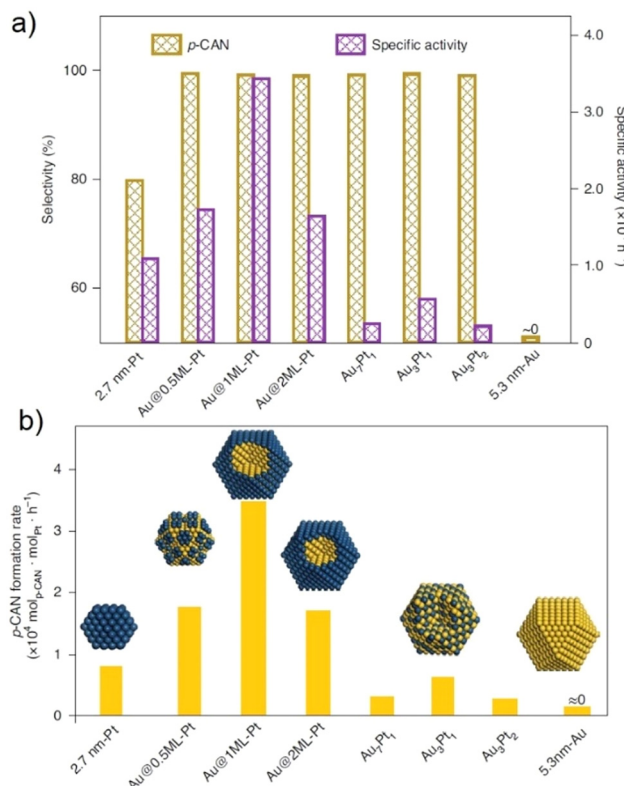


Fig. 4 (a) Comparison of selectivity to *p*-CAN and specific activities of Au@Pt core–shell and AuPt alloy bimetallic catalysts with 2.7 nm-Pt and 5.3 nm-Au monometallic catalysts. (b) Comparison of the *p*-CAN formation rates on the platinum, gold, AuPt alloy and Au@Pt core–shell catalysts. Reproduced from ref. 64 with permission from Springer Nature, copyright 2021.

phous structures and with Cu@Au core–shell particles using icosahedral clusters. The CO binding energies are much more sensitive to the structure of the Cu–Au clusters than to their composition. This is due to the similar strength of CO adsorption on pure Cu and Au. As shown in Fig. 6, icosahedral clusters consisting of pure Cu, pure Au, or with an Au-core–Cu-shell composition adsorb CO molecules strongly compared to other clusters. In addition, icosahedral clusters with a Cu@Au core–shell composition exhibit a more restricted range of CO binding energies compared with fcc and amorphous clusters. Furthermore, amorphous clusters exhibit weaker binding of CO molecule than fcc clusters for a pure Au composition, but conversely stronger binding for clusters with an Au core and Cu shell. In general, the observed adsorption properties are subject to cluster structures that are difficult to predict.

Changing the core–shell size ratio in a nanoparticle can significantly affect the redistribution of the surface charge. The charge redistribution effect should be considered when considering potential applications of nanoparticles in catalysis, as the adsorption of different molecules is strongly dependent on the charges present on their surface. In particular, the CO molecule adsorbs *via* the donor mechanism and involves positively charged sites for adsorption.^{74,75} By modifying the struc-

ture and composition of nanoparticles the redistribution of surface charge can be precisely altered, offering significant prospects for their application in various fields. Chepkasov *et al.*⁶² studied the redistribution of charge on the surface of PtPd nanoparticles with 321 atoms (2 nm diameter) and different structures were selected to study their electronic properties. Several Pt core/Pd shell clusters (from 10 to 50% Pt) were studied. Likewise, the Pd core/Pt shell structure showed a variation of Pt content from 90 to 50%. Five different bimetallic alloy Pt–Pd NPs with random atomic distribution were studied (from 10 to 90% Pt).

Fig. 7a shows the variation in surface charge between pure Pt and Pd nanoparticles, which is 0.015e. This value is consistent with the variance in the work functions of the two atoms (*e.g.* Pt and Pd).⁷⁶ The surface of the nanoparticles is consistently negatively charged, with the exception of the cubic Pt@Pd particles, which have a small positive surface charge of +0.0015e, as shown in Fig. 7a. Pt@Pd and Pd@Pt nanoparticles show opposite trends, specifically in terms of the shift of the Pt–Pd (Pd–Pt) interface from the center to the particle surface. However, the number of surface electrons in Pd@Pt nanoparticles increases in proportion to the decrease in the number of Pt layers surrounding the Pd core, and *vice versa*. It can be concluded that the addition of a monoatomic layer of Pt atoms to Pd nanoparticles can double the surface charge compared to a pure Pt particle, or triple it compared to the surface of Pd nanoparticles. These results are consistent with previous findings suggesting that charge transfer in core–shell Pd@Pt nanoparticles occurs from Pd to Pt.^{77,78} Although enhanced catalytic activity of Pt atoms in nanoparticles, such as in the oxygen adsorption reaction, is related to their ability to donate electrons to oxygen,⁷⁹ excess electron density localization on the nanoparticle surface can also lead to enhanced catalytic activity.^{80,81} Conversely, a different scenario is observed when Pt nanoparticles are coated with a monoatomic layer of Pd. As Pd tends to predominantly occupy the surface of the nanoparticles upon heating, it is crucial to carefully consider the application. In this scenario, palladium acts as a screen reducing the surface charge in the nanoparticles.

The study of the electronic properties of Ih PtPd nanoparticles revealed an increase in the average surface charge compared to fcc PtPd nanoparticles. According to calculations, the increase of the average surface charge for Ih monodisperse nanoparticles of Pt and Pd compared to the fcc structure is 27% (from $-0.0357e$ for Pt_{fcc} to $-0.0454e$ for Pt_{Ih}) and 39% (from $-0.0208e$ for Pd_{fcc} to $-0.0289e$ for Pd_{Ih}), respectively. Among all the studied nanoparticles, the largest excess of electronic density at the surface was observed in the Ih particles, where the Pd core was covered by a monolayer of Pt, and the average surface charge increased by 18% (from $-0.0635e$ for Pd@Pt_{fcc} to $-0.0749e$ for Pd@Pt_{Ih}) (see Fig. 5). For the Ih particles with a Pt core covered by a Pd monolayer, the charge changes from +0.0015e for Pt@Pd_{fcc} to $-0.0001e$ for Pt@Pd_{Ih} (Fig. 7b).

Recently it has been shown that the particle structure affects the surface charge redistribution in AuCu nanoparticles (NPs).⁸² Bader's theory was used to study the surface charge

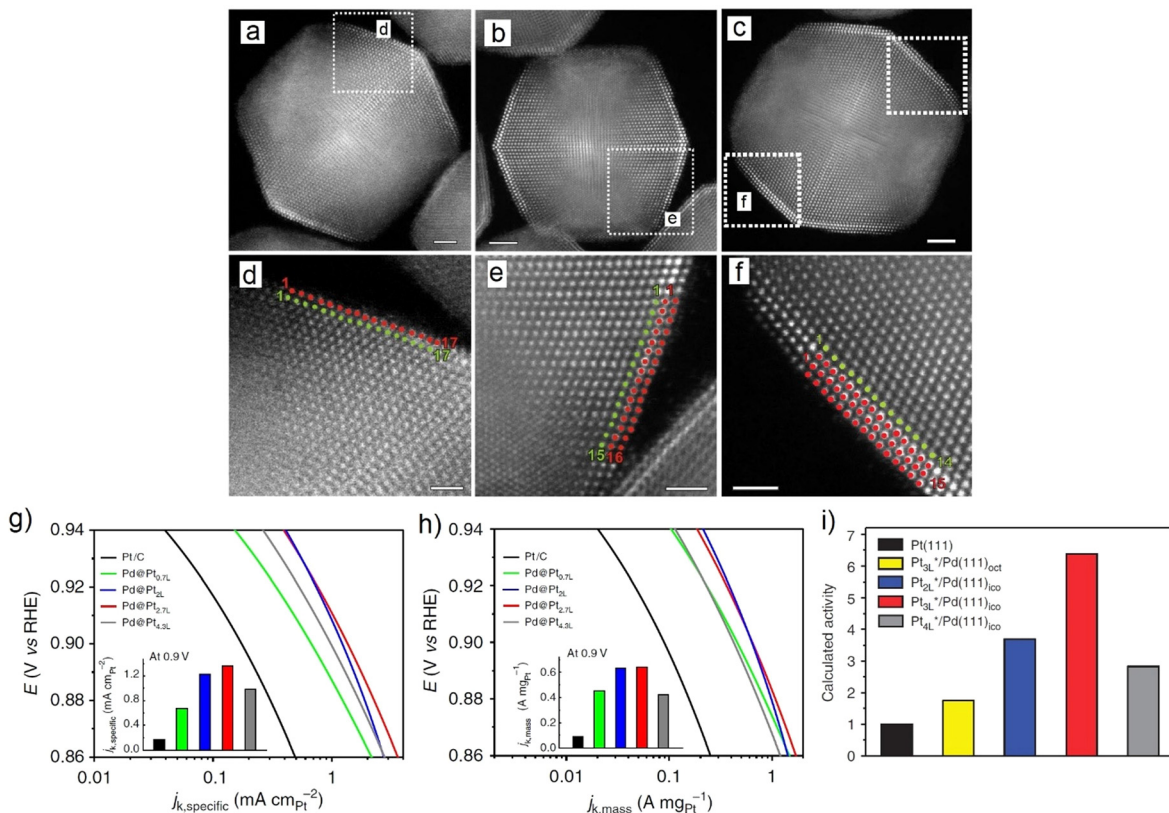


Fig. 5 (a–f) Atomic resolution HAADF-STEM images of Pd@Pt nanoparticles with 1, 2, and 2.7 layers of Pt shell. (g and h) The specific and mass oxygen reduction reaction (ORR) activities are expressed as kinetic current densities (j_k) normalized with respect to the electrochemically active surface areas (ECSAs) and Pt masses of the catalysts, respectively. (i) DFT calculations were used to analyze the ORR activity of the $\text{Pt}_n\text{L}^*/\text{Pd}(111)_{\text{ico}}$ slab models. Relative specific activities of $\text{Pd@Pt}_n\text{L}$ icosahedra at 0.9 V versus (vs.) RHE calculated using the $\text{Pt}_n\text{L}^*/\text{Pd}(111)$ icosahedral slab models, denoted as $\text{Pt}_n\text{L}^*/\text{Pd}(111)_{\text{ico}}$, at a tensile strain of 2.4% for the Pd surface. For comparison purposes, the result for $\text{Pt}_3\text{L}^*/\text{Pd}(111)_{\text{oct}}$ is also included. All the values are given relative to the pure Pt(111) surface. Reproduced from ref. 37 with permission from Springer Nature, copyright 2015.

distribution in core–shell and bimetallic alloy AuCu NPs with diameters of 2 nm (321 atoms) and fcc, icosahedral, and amorphous structures. The study demonstrates that uniform Cu–Au alloys (fcc, Ih, and amorphous) consistently exhibit an excess of electrons, with an average surface charge of approximately $-0.025e$ per surface atom (as shown by the blue lines in Fig. 8a–c). The results indicate that the atom-thick Au shell of the Cu core (green lines in Fig. 8a–c, corresponding to the composition of $\text{Cu}_{0.5}@\text{Au}_{0.5}$) has an average surface charge four times higher than that of a pure metallic NP of the same size ($-0.1e$ and $-0.025e$ per surface atom, respectively). The surface charge of the atom-thick Cu shell of the Au core ranges from approximately $-0.025e$ to $0.075e$ per surface atom (as shown by the red lines in Fig. 8a–c), depending on the Cu : Au composition. The surface charge for Au NPs with both fcc and Ih structure types is larger compared to pure Cu NPs. Specifically, it is $-0.0193e$ compared to $-0.0179e$ for fcc and $-0.0272e$ compared to $-0.0191e$ for Ih (see Fig. 8a–c). This result is in good agreement with the difference in the work functions for these atom types.⁷⁶

However, in the case of the amorphous structure of nanoparticles (NPs), the situation is reversed. For pure gold (Au)

NPs, the charge is $-0.0196e$, while for copper (Cu) NPs, the charge is $-0.0205e$. According to the authors, this effect is probably due to the highly deformed surface of amorphous NPs. The charge difference also indicates a tendency for the electron density to be redistributed from the copper atoms to the gold atoms. It can be concluded that changing the ratio of atoms in the core and shell of the particle, as well as the type of metal on the surface (Au or Cu), has a significant impact on the surface charge:

1. The Cu core covered by an atom-thick Au shell exhibits a significant excess of electrons flowing from the copper atoms to the surface gold atoms, resulting in a negative charge on the NP surface;

2. The Au core covered by an atom-thick Cu shell shows the opposite effect, resulting in a deficiency of electrons on the surface and a positive charge.

Therefore, modifying the structure of the AuCu nanoparticles allows for precise adjustment of the surface charge, thereby broadening their potential applications.

A successful descriptor for determining catalytic properties is the *d*-band center. Chepkasov *et al.*⁸² calculated the *d*-band center for all AuCu NPs considered by projecting the electronic

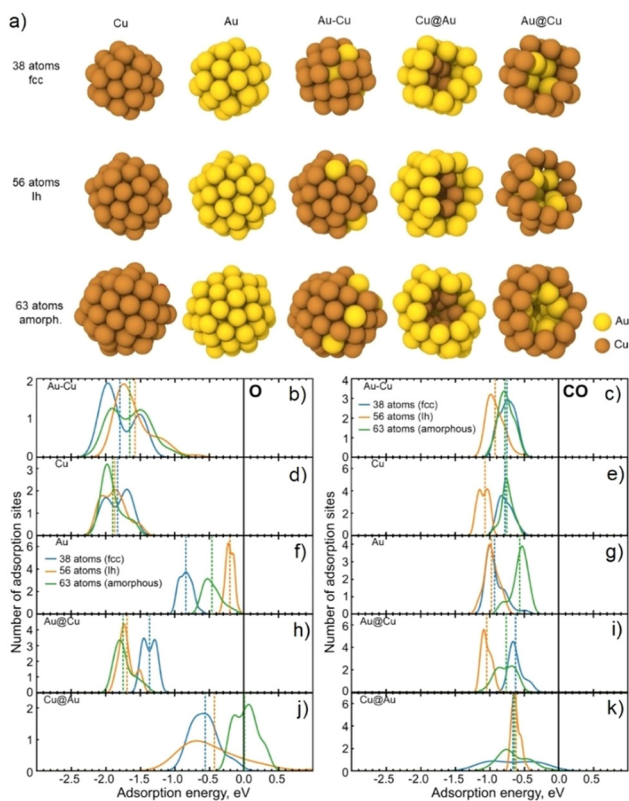


Fig. 6 (a) View of nanoparticles with different atomic structure. (b–k) Distributions of adsorption energies of O and CO species calculated for (b and c) fcc, $\text{Cu}_{34}\text{Au}_4$ icosahedral, $\text{Cu}_{50}\text{Au}_6$, and amorphous $\text{Cu}_{56}\text{Au}_7$ clusters from MD simulations;⁷³ distribution for the same cluster structures composed of pure Cu (d and e), pure Au (f and g), Au@Cu (h and i), and Cu@Au (j and k). The distributions were obtained by applying 0.35 eV smearing to the calculated adsorption energies. The dashed lines reflect the average adsorption energies calculated for each distribution. Reproduced from ref. 73 with permission from John Wiley & Sons, Inc., copyright 2022.

densities of states onto each atom in the NP. Only the surface atoms were selected for analysis, and the surface *d*-band center values were averaged. The authors calculated that the average surface *d*-band center for Au is -3.22 , -3.28 , and -3.32 eV for the fcc, icosahedral, and amorphous structure types, respectively (Fig. 8d–f). For Cu surfaces, the average *d*-band centers were -2.32 , -2.41 , and -2.35 eV for the fcc, icosahedral, and amorphous structure types, respectively. The authors concluded that the structure type of the NP slightly influences the *d*-band center.

Core–shell structures consist of a Cu or Au core covered by an atom-thick shell (Au or Cu atoms respectively). These structures exhibit the maximum or minimum values of the *d*-band center among all other NPs. For Au@Cu NPs, the maximum values for Au : Cu = 1 : 1 are about -2.11 , -2.14 , and -2.16 eV for the fcc, icosahedral, and amorphous structures, respectively. Cu@Au NPs, on the other hand, exhibit minimum values of the *d*-band center of -3.55 , -3.77 , and -3.42 eV for the fcc, icosahedral, and amorphous structures, respectively.

Compared to the core–shell NPs, the alloy particles exhibit a monotonic decrease in the dependence of the *d*-band center on the Au concentration (blue lines in Fig. 8d–f). The icosahedral Cu@Au (green line Fig. 8d–f) exhibited the smallest *d*-band center value of -3.77 eV among all other NPs, corresponding to the core–shell Cu@Au NP with almost 50% gold in the composition. Jiao *et al.*⁸³ showed that a lower *d*-band center value results in a weaker binding energy between adsorbents and the metal surface. However, the Sabatier principle suggests that the adsorption energy should be neither too strong nor too weak for optimal interaction between the adsorbent and catalyst surface. Therefore, modifying the ratio of core and shell atoms in AuCu NPs can significantly alter their surface properties, including the *d*-band center.

Based on the above, the authors investigated the effect of changing the particle structure on the adsorption properties of CuAu nanoparticles. For this study, the fcc structure type was chosen as a model system to demonstrate general tendencies in the adsorption of O and CO on the AuCu NPs. In order to investigate the influence of the local atomic environment of AuCu NPs on the adsorption energy of O and CO, 14 different adsorption sites on the surface of AuCu nanoparticles with fcc structure were considered. The selected adsorption sites included top, bridge, hollow, and kink to ensure a comprehensive adsorption pattern. The adsorption energies of oxygen and carbon monoxide on the copper-terminated surface of Au@Cu nanoparticles were found to be lower than those of Cu@Au nanoparticles with a gold surface. The presence of gold on the surface prevents oxidation of the nanoparticles, avoiding oxygen poisoning and allowing better adsorption of CO. From a different perspective, this behaviour can inhibit CO oxidation by both Langmuir–Hinshelwood and Eley–Rideal mechanisms. In contrast, Au@Cu nanoparticles are well suited to reactions that follow these mechanisms.

To visually represent the change in adsorption energy based on the local atomic environment and composition, we plotted the dependence of the average adsorption energy of O and CO on these properties, as shown in Fig. 8g and h. The difference between the adsorption energies of O and CO on the surfaces of pure Cu and Au nanoparticles is 1.92 eV (-1.48 eV for Cu NP and 0.44 eV for Au NP). The adsorption energy of Au@Cu particles decreases as the concentration of gold in the core increases and the thickness of the copper shell decreases. Specifically, the adsorption energy decreases from -1.48 eV for pure Cu NP to -1.65 eV for Au@Cu with an atom-thick Cu shell.

Similarly, for Cu@Au NPs, a decrease in the number of Au atoms in the shell results in a decrease in the adsorption energy of oxygen atoms. The adsorption energy value decreases from 0.44 eV for pure Au NP to 0.23 eV for Cu@Au with an atom-thick Au shell, although it remains positive.

A recent study of the surface properties of core–shell PdAu nanoparticles⁸⁴ observed similar effects of charge and *d*-band center changes depending on the particle structure. It was found that homogeneous Au–Pd alloys always have an excessive negative charge in the range of from -0.016 to $-0.03e$.

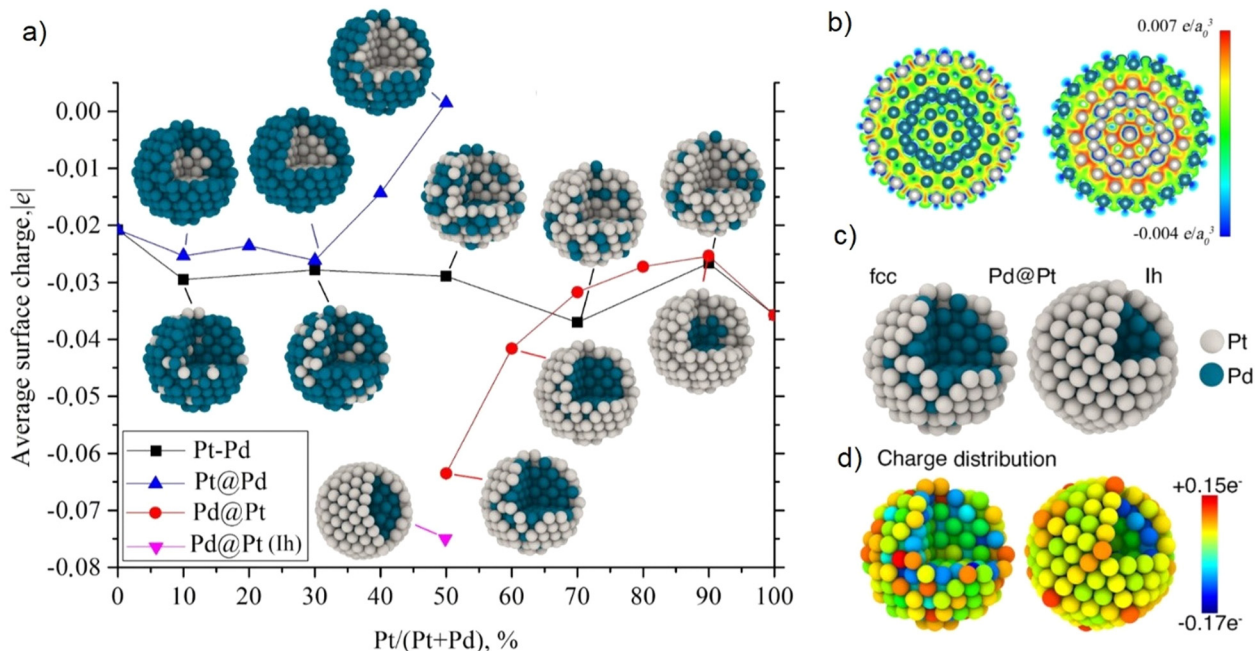


Fig. 7 (a) Average surface charge of the Pt–Pd nanoparticles vs. Pt content. (b) The difference in electron density between the Ih structures of Pd@Pt (left) and Pt@Pd (right) determined by superimposing the atomic densities of their constituent atoms. (c and d) View of structures and charge distribution in Pd@Pt nanoparticles with an fcc and Ih structure. Reproduced from ref. 62 with permission from the American Chemical Society, copyright 2018.

The type of metal in the shell/core determines the excess of electrons on the surface. The surface charge of Pd@Au nanoparticles is more negative (to $-0.03e$), while that of Au@Pd nanoparticles is less negative (to $-0.005e$). This phenomenon was observed due to the smaller work function of Au compared with Pd. The localization of electron density is shifted from the Pd atoms to the region close to the subsurface Au atoms, as shown in Fig. 9d for Au@Pd nanoparticles.

In contrast to Pd@Au, we observed a lower degree of charge distribution (see Fig. 9d). It is important to consider the effect of charge redistribution when applying nanoparticles in catalysis, as different molecules require different surface charges for adsorption. Specifically, the CO molecule adsorbs through the donor mechanism^{85,86} and requires positively charged sites for adsorption. Thus, altering the structure and composition of nanoparticles allows for precise control over the redistribution of surface charge. This presents exciting opportunities for their application in various fields.

The surface charge behavior and *d*-band center can be explained by the variation of the shell lattice parameter depending on the core in the nanoparticle's composition. Specifically, in the case of Pd@Au nanoparticles, the interatomic distance on the surface changes from 2.792 Å for pure Au nanoparticles to 2.780 Å for Pd₁₃₅@Au₁₈₆ (57.94% Au) nanoparticles (Fig. 9c). Changes in the interatomic distance affect the surface properties of core-shell nanoparticles. Changes in the charge and *d*-band center impact the adsorption of O and CO on the surface of PdAu core-shell nanoparticles. Specifically, the adsorption energies of O and CO on

the surface of Au@Pd nanoparticles are lower than those for Pd@Au nanoparticles with an Au surface (see Fig. 9a and b). Minor fluctuations in the energy of adsorption for both O and CO are observed when the size ratio of the core and shell is altered.

Core–shell nanorods

In addition to core–shell nanoparticles, other core–shell nanocatalysts have been actively used in catalysis. In particular, Hoeven *et al.*³⁴ showed that by changing the atomic distribution in core–shell Au–Pd nanorods, a synergistic effect can be achieved in the selective hydrogenation of butadiene on an industrially relevant scale. The selective hydrogenation of 1,3-butadiene is the most important reaction for the purification of alkene feedstocks for the polymer industry. The problem is the selective conversion of polyolefins without the hydrogenation of mono-olefins, which are present in large excess. Pd-based materials are active catalysts for hydrogenation because hydrogen readily dissociates on the Pd surface^{87,90} and at low conversions Pd catalysts can be quite selective.⁸⁸ However, near full conversion the hydrogenation of mono-olefins becomes more important.⁸⁹ By combining Pd with a less active and more selective metal, such as Au, or by poisoning it with sulfur, excess hydrogenation can be suppressed,^{30–33} but not without a reduction in activity compared with pure Pd.^{91,92}

Hoeven *et al.*³⁴ designed a model catalyst consisting of Au–core–Pd–shell nanorods coated with a protective mesoporous silica shell. The Au nanorods have a single crystal face-centered cubic (fcc) structure with {110} and {100} facets exposed

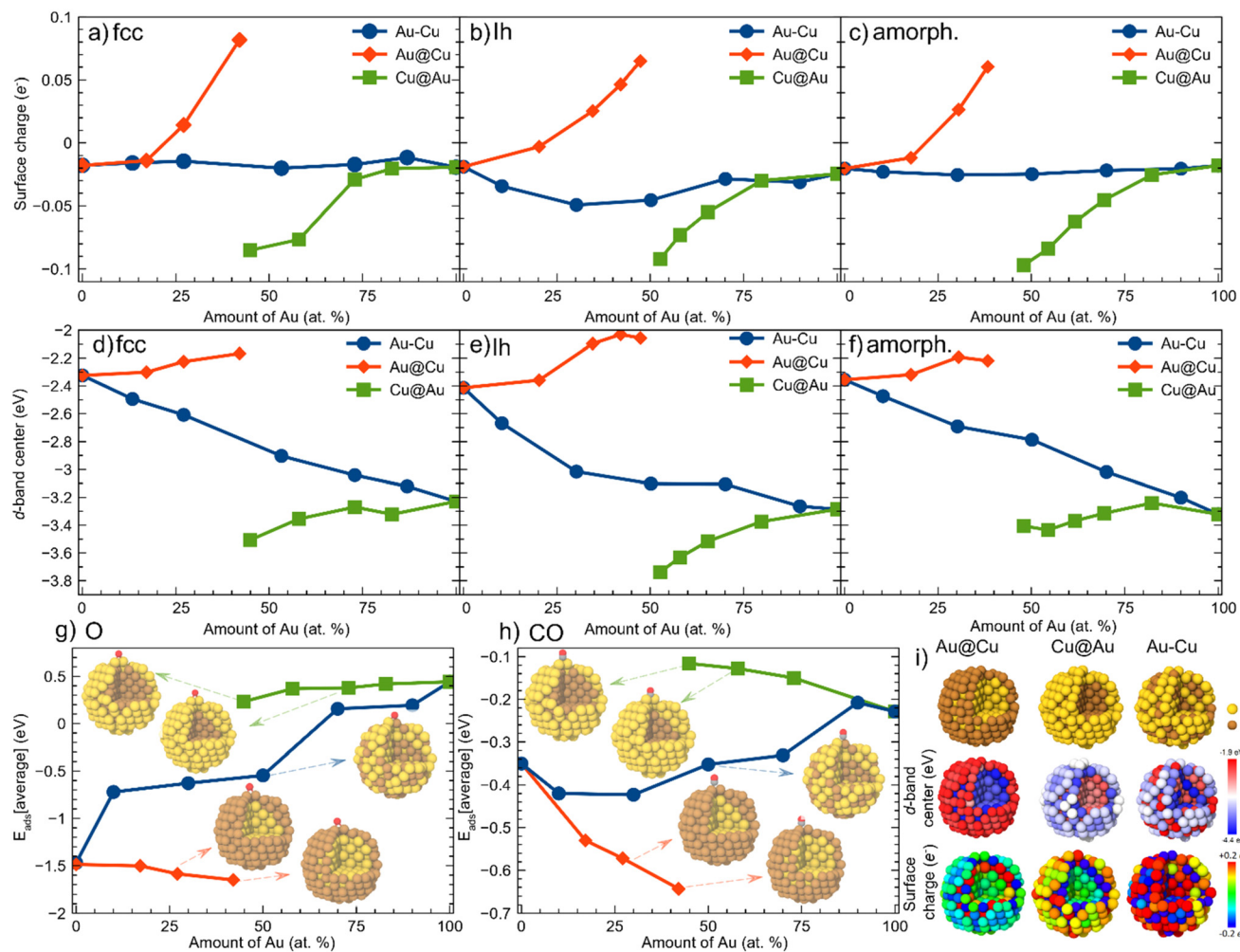


Fig. 8 (a–c) Average surface charge of AuCu NPs with different structures (fcc, Ih and amorphous) and atomic environments (Cu@Au, Au@Cu, and Au–Cu) as a function of composition. Positive values indicate a shortage of electrons (electrons have migrated from the surface to the interior), and negative values indicate an excess of electrons resulting in a negative surface charge. (d–f) d-Band centers averaged over the surface of AuCu nanoparticles with fcc, Ih and amorphous structure types and atomic environments (Cu@Au, Au@Cu, and Au–Cu) as a function of composition. (g and h) Average adsorption energy of O and CO on AuCu NPs with different local atomic environments (Cu@Au, Au@Cu, and Au–Cu) as a function of composition. (i) Atomic structures of fcc nanoparticles with atomic charge distributions and spatial distributions of d-band center values. The gold and copper atoms are shown by yellow and brown spheres, respectively. Reproduced from ref. 82 with permission from the American Physical Society, copyright 2023.

along the length of the rod.⁹³ The Pd shell thickness was varied by changing the Pd precursor, resulting in Au@Pd@SiO₂ nanorods with atomic Pd fractions X_{Pd} = 0.04, 0.08, 0.21 and 0.32 corresponding to the number of Pd layers, N_{Pd} = 1, 2, 5 and 6 Pd layers, respectively (Fig. 10). The catalytic performance of the Au@Pd@SiO₂ nanorods was tested in the selective hydrogenation of butadiene to butene in the presence of an excess of propene. The catalytic activity is given as the turnover frequency (TOF), which is expressed as the number of butadiene molecules converted per second per metal surface atom. Selectivity was defined as the number of hydrogen molecules used to convert butadiene to butene divided by the total number of hydrogen molecules consumed. It was shown that the core–shell nanorods exhibited high selectivity and a highly reproducible catalytic performance.

Fig. 10 shows that the bimetallic core–shell nanorods outperformed the monometallic Au and Pd catalysts and that the catalytic performance was highly sensitive to the Pd shell thickness. The best combined activity and selectivity for the structures was obtained with the core–shell catalyst with N_{Pd} = 6, where the TOF was 50 s⁻¹ at 45 °C and the selectivity was 80% at 98% butadiene conversion. Thus, tuning the core–shell nanocatalyst structure can lead to a 50-fold increase in activity without losing the high selectivity.³⁴

Core–shell nanocubes

Another nanostructure actively used in catalysis is the nanocube. Xei *et al.*⁹⁴ developed a technique for the deposition of Pt in the form of homogeneous ultrathin shells on Pd nanocubes. This technique allowed the deposition of different

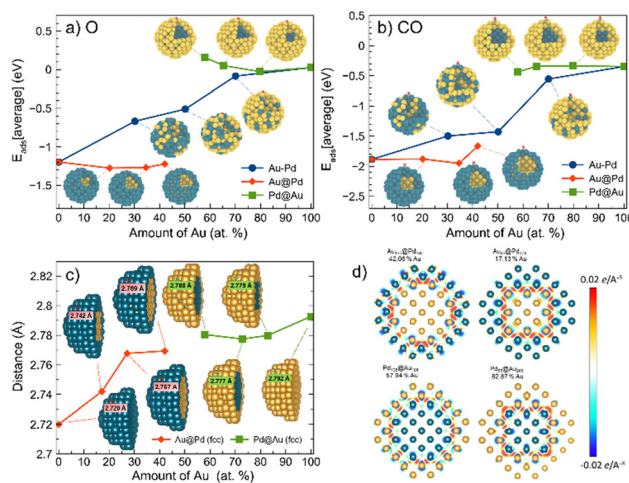


Fig. 9 (a and b) Average adsorption energy of O and CO on PdAu NPs with different local atomic environments (Pd@Au, Au@Pd, Pd–Au) as a function of composition. (c) Interatomic distance between the surface atoms of the considered clusters depending on the composition. (d) Charge transfer between Pd and Au atoms in Pd@Au, Au@Pd nanoparticles visualized as a difference between the electron density of the core and shell. Red areas correspond to density build-up, blue to depletion. (For interpretation of the references to color in this figure legend, the reader is referred to the web version of this article). The Pd and Au atoms are shown by dark blue and yellow spheres, respectively. Reproduced from ref. 84 with permission from the Royal Society of Chemistry, copyright 2023.

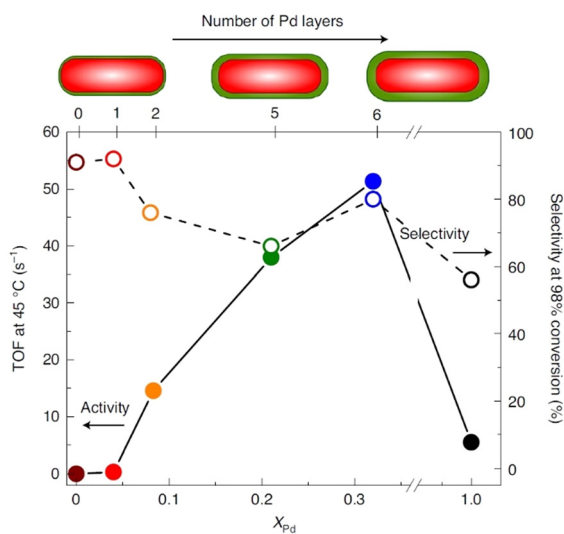


Fig. 10 The catalytic performance of Au-core–Pd-shell catalysts is highly sensitive to the number of shell layers. Au@Pd@SiO₂ NRs with a variable Pd content and shell thickness were used: X_{Pd} = 0.04, N_{Pd} = 1 (red); X_{Pd} = 0.08, N_{Pd} = 2 (orange); X_{Pd} = 0.21, N_{Pd} = 5 (green); X_{Pd} = 0.32, N_{Pd} = 6 (blue); and Au@SiO₂ (X_{Au} = 1.0, brown) and Pd@SiO₂ (X_{Pd} = 1.0, black) reference samples containing spherical 3.0 and 6.1 nm particles, respectively. Activity expressed as TOF (s⁻¹) at 45 °C (left axis) and the selectivity at 98% butadiene conversion (right axis) as a function of the atomic Pd fraction. Reproduced from ref. 34 with permission from Springer Nature, copyright 2021.

numbers of Pt atomic layers (from 1 to 6) on the Pd nanocube, see Fig. 11. Compared with commercial Pt/C catalyst, core-shell Pd@Pt_nL nanocubes ($n = 1$ –6) show an improvement in specific activity and durability in the oxygen reduction reaction (ORR). DFT calculations performed on the model surface (100) suggest that the increase in specific activity can be attributed to the weakening of OH binding due to ligand and strain effects, resulting in an increase in the OH hydrogenation rate. A volcano-like relationship between the ORR specific activity and the number of Pt atomic layers was obtained, which is in good agreement with the experimental results. Both theoretical and experimental studies show that the ORR specific activity is maximum for catalysts based on Pd@Pt₂–3L nanocubes. Due to the decrease in Pt content and increase in specific activity, Pd@Pt₁L nanocubes showed Pt mass activity with an almost three times increase compared with Pt/C catalyst (Fig. 11).

It is also possible to modify the catalytic activity of nanocubes by changing the lattice strain of the shell. In the recent work of He *et al.*³⁹ it has been shown that when ultrathin Pt shells are deposited on palladium-based nanocubes, expansion and shrinkage of the nanocubes by phosphorization and dephosphorization induces a strain in the Pt(100) lattice that can be adjusted from –5.1 to 5.9 per cent. It has previously been shown that the introduction of phosphorus (P) into the lattice of palladium (Pd) nanocubes leads to an increase in the size of the nanocubes, whereas the extraction of P from Pd–P leads to a decrease in the original size of the nanocubes.⁹⁵

This allows the size of the Pd-based nanocubes to be reversibly changed in the range 17.3–20.6 nm by phosphorylation/dephosphorylation, and a wide range of continuous and uniform surface tensions to be set in the platinum (Pt) shells deposited on the nanocubes. To generate lattice strain in Pt shells, Pt is first deposited on Pd nanocubes and then P is introduced into the Pd lattice to expand the Pd core. Lattice contraction occurs when Pd–P nanocubes are used as the initial substrate for Pt deposition, followed by Pt extraction which compresses the Pd core. Since the degree of Pt lattice expansion/contraction is proportional to the degree of phosphorylation/dephosphorylation of the Pd-based nanocubes, which is easily adjustable, the Pt lattice strain can be smoothly tuned between the extreme values maintained by the system. Compared to many other conventional substrates, Pd-based

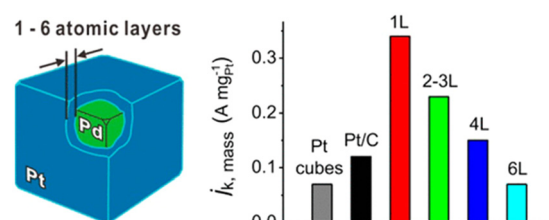


Fig. 11 Scheme Pd@Pt_nL nanocubes and comparison of mass activities given as kinetic current densities (j_k) at 0.9 V (vs. RHE) for the Pt/C and Pd@Pt_nL/C catalysts. Reproduced from ref. 94 with permission from the American Chemical Society, copyright 2019.

nanocubes have the advantage that the same standard distance between the Pd and Pt lattices allows us to precisely control the thickness and orientation of the Pt shell grown on Pd-based substrates, thereby ensuring uniform strain applied to all open areas of Pt.

As experimental results³⁹ show, Pt lattice strain has a strong effect on catalytic activity in terms of specific and mass activities. The curves of specific and mass activities are M-shaped, with peak activities for the methanol oxidation reaction (MOR) seen for Pt lattice strains of -3.9% and 4.7% , respectively. This suggests that both lattice tension and lattice compression can enhance the catalytic performance of Pt towards the MOR, but excessive strain reduces the catalytic activity. $\text{Pt}_{\text{T}-4.7}$ is the most active catalyst, with specific and mass activities as high as $12.82 \text{ mA cm}^{-2} \text{ Pt}$ and $2.94 \text{ mA } \mu\text{g}^{-1} \text{ Pt}$ at 0.65 V *vs.* silver/silver chloride (Ag/AgCl), which are approximately $2.3/2.5$ times greater than those of Pt_0 and $18.8/6.7$ times greater than those of Pt/C , respectively. It was also found that Pt shells show a significant strain dependence when catalyzing the hydrogen evolution reaction (HER). A volcanic strain-activity relationship was found for this reaction. The best performing catalyst, $\text{Pt}_{\text{T}-2.8}$, achieves specific and mass activities up to $22.71 \text{ mA cm}^{-2} \text{ Pt}$ and $5.02 \text{ mA } \mu\text{g}^{-1} \text{ Pt}$, respectively, at -0.07 V *versus* a reversible hydrogen electrode, which are substantially improved compared with those of Pt_0 and are about 12.3 and 4.4 times greater than those of Pt/C .

Zhu *et al.*⁹⁶ demonstrated a method for the facile synthesis of $\text{Pd}@\text{Ir}_{n\text{L}}$ (n : the number of Ir atomic layers) core–shell nanocubes with a controlled shell thickness from one to four atomic layers. The catalytic activity of these nanocatalysts was tested on the oxygen extraction reaction (OER), since Ir is known to be a key companion of the most efficient OER electrocatalysts.^{97–99} However, Ir has an extremely low abundance in the Earth's crust. For an Ir-based electrocatalyst to be cost effective, it is necessary to maximize its mass activity by increasing both the specific activity and the utilization efficiency of the Ir atom. The OER activities of $\text{Pd}@\text{Ir}_{n\text{L}}$ nanocubes showed a volcano-type dependence on the number of Ir atomic layers, with a maximum corresponding to $n = 3$. Due to the better passivation for the Pd cores and the formation of a more stable phase during electrolysis, the $\text{Pd}@\text{Ir}_{n\text{L}}$ nanocubes with thicker Ir overlayers exhibited greater OER durability. The $\text{Pd}@\text{Ir}_{3\text{L}}$ nanocubes provided the best activity and durability against the OER with η as low as 245 mV at $10 \text{ mA cm}_{\text{geo}}^{-2}$ and a mass activity of $3.33 \text{ A mg}_{\text{Ir}}^{-1}$ at $\eta = 300 \text{ mV}$ (Fig. 12). Both values were much better than those of commercial Ir/C and represent the best data set among the Ir-based core–shell OER catalysts in acidic media.

Descriptors for the evaluation of adsorption

Adsorption is one of the key processes that determine the reaction pathway.¹⁰⁰ For example, the adsorption energies of O_2 and CO determine the mechanism of the CO oxidation

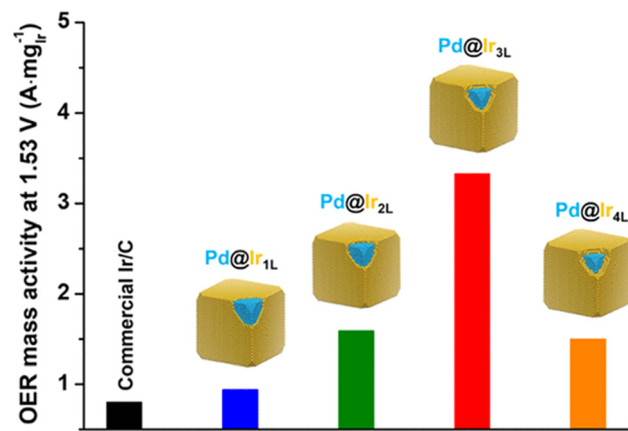


Fig. 12 Mass activities at $\eta = 300 \text{ mV}$ of $\text{Pd}@\text{Ir}_{n\text{L}}/\text{C}$ compared with the commercial Ir/C catalyst. Reproduced from ref. 96 with permission from the American Chemical Society, copyright 2014.

reaction.^{101–103} Also, by studying the adsorption process of the reactants and some of the intermediates one could tune the catalytic activity of the material or the reaction conditions to avoid poisoning of a catalyst.^{104,105} The adsorption of different molecules on the catalyst surfaces is therefore very important in many manufacturing processes.

Since experimental studies are time-consuming, modern scientists often use computer modelling based on density functional theory (DFT), as implemented in many software packages.^{106–111} However, DFT calculations require a lot of computational resources, and the high-throughput search for a suitable catalyst or adsorption site with the lowest adsorption energy becomes a challenge. Therefore, many simplifications are used to describe the specific properties of nanoparticles responsible for their catalytic activity. Nanoparticles made of different chemical elements have a high degree of freedom in atomic configuration, composition, size, and shape, and some of them also have strain effects, leading to different adsorption properties. All these features of the material should be described by a well-functioning simplified model called a descriptor.

Different descriptors based on the constitutional,^{112–114} geometric,^{115–120} electronic,^{83,112,117,121–124} optical,¹²⁵ and quantum chemical properties^{112–114,126} of the catalytic materials and thermodynamic^{124,126–128} and kinetic^{127,129} properties of the adsorption process have been successfully applied to study the catalytic processes. All known descriptors that allow the determination of valuable properties of a catalyst are shown in Fig. 13.

Generalized coordination number

In contrast to the usual coordination number (cn), which only takes into account the nearest neighbors of a given atom, the generalized coordination number ($\overline{\text{CN}}$) is first-order extension of it, which takes into account the second nearest neighbors of active sites.¹¹⁹ The difference between the cn and $\overline{\text{CN}}$ is shown in Fig. 14a.

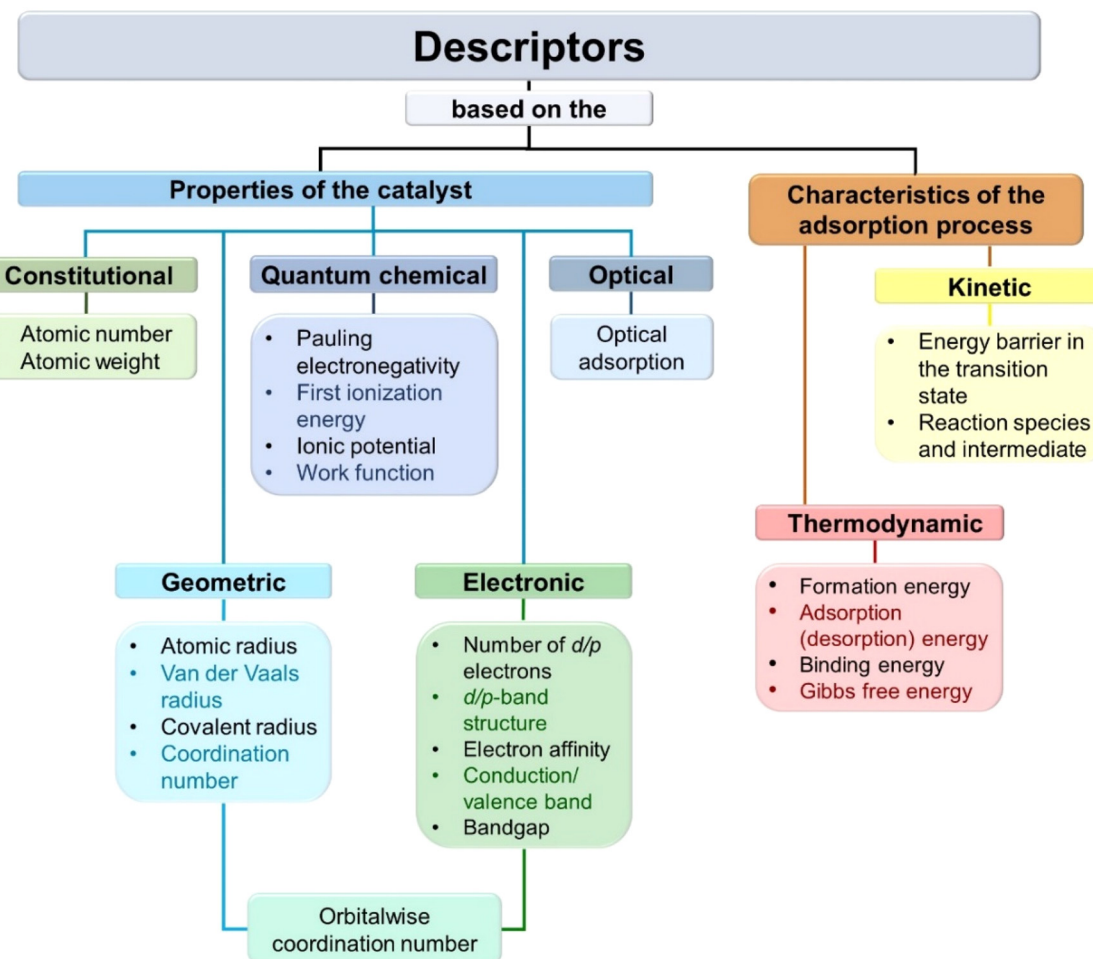


Fig. 13 Block-scheme showing the different descriptors based on the properties of the catalytic material and the characteristics of the reaction processes.

There is a linear correlation between the adsorption energy and \overline{CN} ,^{119,120} which can describe the difference in catalytic activity between different size nanoparticles¹³⁰ as shown in Fig. 14b and c. Instead of the simplicity of this descriptor it has been successfully used to describe the adsorption on many alloys and nanoparticles.^{131–134}

Nevertheless, the use of the generalized coordination number cannot account for the consideration of different surface reconstructions, as it includes numerous different configurations, making the solution of this case too complex. Furthermore, studies on the application of the generalized coordination number are limited to monometallic systems. However, Nanba and Koyama¹³⁵ have successfully refined this approach and made it possible to apply it as a descriptor for alloys of Pt_3M ($M = Co, Ni, or Cu$).

Orbitalwise coordination number

As mentioned above, the generalized coordination number is not sufficient to describe multi-metal systems. In addition, different alloys may have the same value of \overline{CN} , but different adsorption capacities due to the properties of each metal.

As the adsorption potential is highly dependent on the electronic structure of the catalyst, it is recommended to refine the geometric descriptors and make them more universal. This has improved the accuracy and universality of the generalized coordination number. Xin *et al.*¹¹⁶ proposed a descriptor called the orbitalwise coordination number, which takes into account the crystal orbital overlap and coordinate saturation of metal atoms, and is based on the moments theorem.¹³⁶

To describe the crystal orbital overlap of an atom coordinating with other atoms, Xin *et al.*¹¹⁶ use the second moment $M_{2,i}^\alpha$, which characterizes the width of the eigenspectrum distribution of the given orbital ($\alpha = s$ or d) and a sum of the squares of the α -electron hopping integrals ($t_{nn}^{\alpha,\infty}$)² to determine the relevant valence orbitals of the first nearest-neighbor atom in the optimized bulk material:

$$CN_i^\alpha = \frac{M_{2,i}^\alpha}{(t_{nn}^{\alpha,\infty})^2}$$

By analyzing the adsorption of CO on different Au atoms of differently shaped nanoparticles, it has been shown that decreasing (increasing) the coordination between neighboring

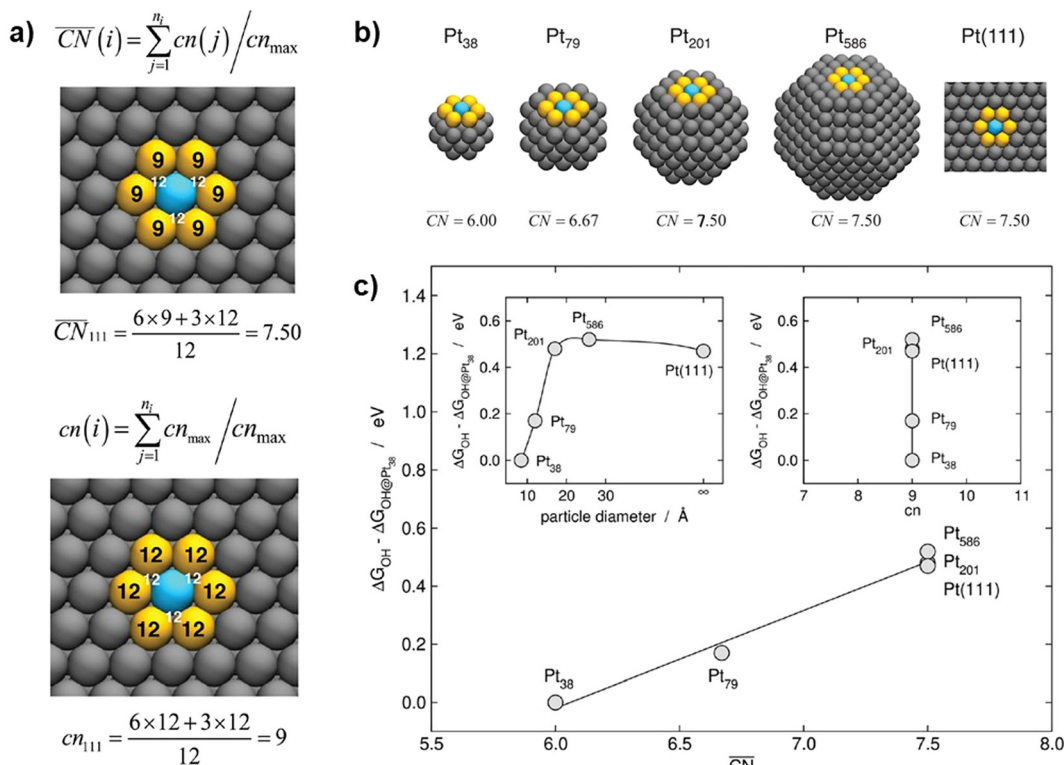


Fig. 14 (a) Evaluation of conventional (bottom) and generalized (top) coordination numbers for a surface atom at a (111) terrace. The atom i for which cn and \overline{CN} are assessed is shown in blue, its first nearest neighbors on the surface layer are shown in yellow, and other surface atoms are in gray. The coordination number of the first nearest neighbors is shown in every case. There are three first nearest neighbors in the subsurface layer which cannot be seen from the displayed top view, but their coordination numbers are provided in white;¹²⁰ (b) different Pt clusters with different \overline{CN} of the second nearest neighbors;¹³⁰ and (c) trends in atop *OH adsorption energies using Pt_{38} as a reference for the sites shown in the top panel. The scalability and extended-surface regimes are shown in the left inset, the limitations of cn to distinguish the sites are shown in the right inset, and the nearly linear description offered by \overline{CN} is shown in the main panel.¹³⁰ Panel (a) reproduced from ref. 120 with permission from John Wiley & Sons, Inc., copyright 2023. Panels (b) and (c) reproduced from ref. 120 with permission from the Royal Society of Chemistry, copyright 2019.

Au atoms, which leads to a smaller (larger) coordination number (CN^S), increases (decreases) the CO adsorption. Comparing Fig. 15a with Fig. 15b, it is clear that calculating the orbitalwise coordination number gives more accurate results.

Thus, the CN^a provides a solid physical basis *via* a direct link to the electronic structure of an adsorption site. This makes it suitable for describing the surface reactivity of metal nanoparticles that differ in size, shape, and composition.

d-Band center

The most widely used descriptor to determine the catalytic activity of metallic nanoparticles is the *d*-band center (ϵ_d), proposed by Nørskov *et al.*^{137–139} It allows one to describe the adsorption possibilities of different surfaces based on the position of the electronic *d*-band of the metal. According to this theory, the closer the *d*-band center to the Fermi level, the stronger the interaction between the surface and the intermediates of the different reactions.⁸³

Calle-Vallejo *et al.*¹¹⁹ derived the almost linear correlation between ϵ_d and \overline{CN} based on the broken-band model.^{140,141} A decrease of the coordination number of the transition metal

(TM) atom leads to a decrease in the *d*-band overlap. It causes the *d*-bandwidth (W_d) to decrease, thus shifting the *d*-band center of the atom towards the Fermi level.^{139,142,143} This process can be described as follows:

$$\epsilon_d^{\text{surf}} \approx \epsilon_d^{\text{bulk}} + \frac{E}{2\theta_d f} \left(\frac{\overline{CN}_{\text{surf}}}{\overline{CN}_{\text{bulk}}} - 1 \right),$$

where ϵ_d^{surf} and ϵ_d^{bulk} are the *d*-band center values of an atom on the surface and in the bulk, respectively, E is the cohesive energy of the material, θ_d is the average occupancy of the *d*-states, and f is an additional ratio factor.

According to the Newns-Anderson model,^{144,145} adsorption on the surfaces could be described as a two-step process. The valence state of the given adsorbate reacts with the *s*-state of the TM, and then the obtained state reacts with the *d*-states of the TM. In contrast to the interaction between the adsorbate and the *s*-states of the TM, the interaction between the adsorbate state and the *d*-states of the TM gives rise to the split-off bonding and antibonding states which are located below and above the original adsorbate state, respectively.⁸³

The *d*-band as a descriptor is not restricted to the composition; it can be used for compositions with a number of different

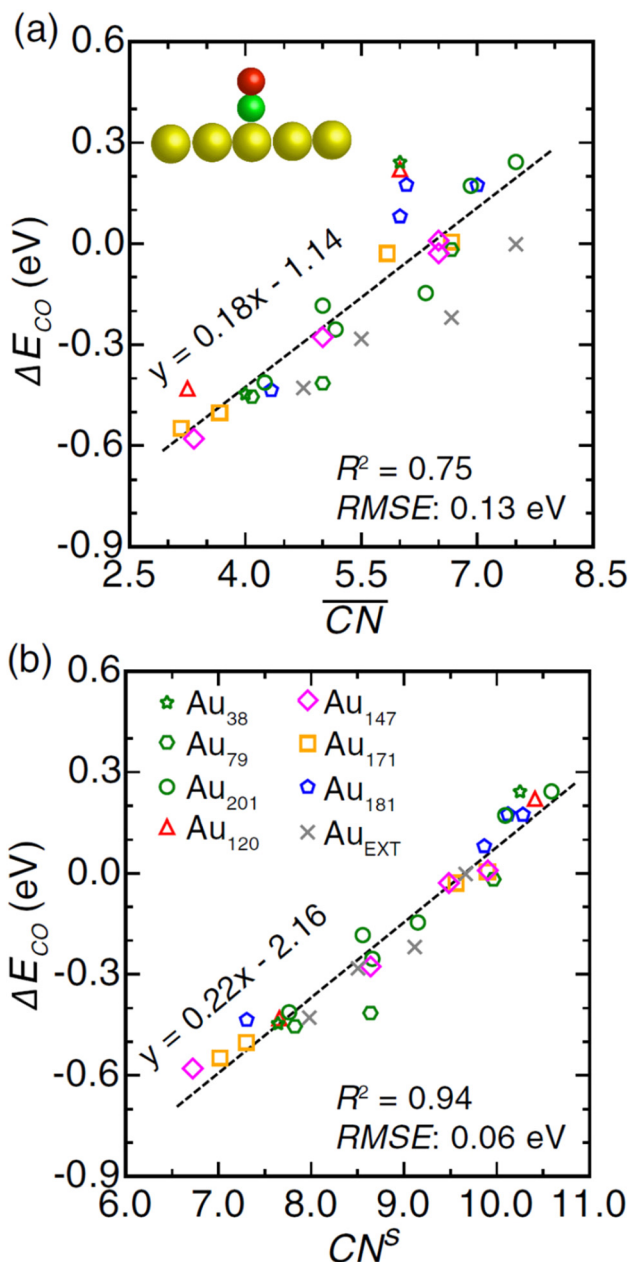


Fig. 15 Adsorption energies of the atop CO on Au nanoparticles and extended surfaces described by (a) the generalized coordination number \overline{CN} ,¹¹⁹ and (b) the orbitalwise coordination number CN^S computed using the two-center s-electron hopping integrals. Linear regression lines (dashed) and related statistics are also given from.¹¹⁶ Panel (a) reproduced from ref. 119 with permission from Wiley-VCH, copyright 2014. Panel (b) reproduced from ref. 116 with permission from the American Physical Society, copyright 2017.

TMs or TMs with the non-metallic elements leading to a shift in the d -band. This shift has been observed in the bulk alloys,^{146–148} TM nanoparticles on the non-metallic substrate,^{149,150} TM species on the metallic substrate,^{151,152} doped materials,^{153,154} decorated surfaces,¹⁵⁵ simple compounds (MX),^{156,157} nanoclusters^{158,159} and nanowires,¹⁶⁰ MOF structures,¹⁶¹ SAACs^{162–166} and the core-shell nanostructures.^{167–170}

The d -band shift can be determined experimentally during the electronic structure study by the commonly used XPS and UPS methods,¹⁵⁹ which study the electron distributions on the surface of the electrocatalyst. Alternatively, X-ray absorption spectroscopy (XAS)¹⁷¹ may be used to determine changes in adsorption energy and electron transfer on the surface.

First-principles simulations can also be used to compute the d -band center shift by calculating the electronic density of states (DOS). Vojvodic *et al.*¹⁷² show that the semi-empirical fits to the DFT-calculated DOS are effective in representing the d -band properties of TMs. Furthermore, the LOBSTER package¹⁰⁸ can be used to determine the changes in the chemical bonding between the adsorbate and the active site to infer the bonding and anti-bonding states and their positions with respect to the Fermi level.¹⁷³

When the spin polarization is taken into account in the calculations, there are two d -band centers – one with spin-up and one with spin-down. The spin-down state ($\epsilon_{d\downarrow}$) is shifted above the unpolarized d -band center, while the spin-up state ($\epsilon_{d\uparrow}$) is shifted below it, as shown in Fig. 16. Each of two the centers has its own bonding and anti-bonding states that react with an adsorbate, resulting in a non-linear dependence of the adsorption energy on the number of d -electrons. As the degree of spin polarization decreases, the two d -band centers move closer together, but at high spin polarization, such centers are shifted in opposite directions, potentially leading to competition between them.¹²¹

The main advantage of the d -band as a descriptor is the ability to tune the properties of a catalyst. Shifting the d -band center downwards reduces the bond strength between the adsorbates and a surface, while shifting it upwards reduces the adsorption energy. This property can be used to modify the reaction rate or pathway. For example, if certain reaction products remain on the surface and cause poisoning, the cata-

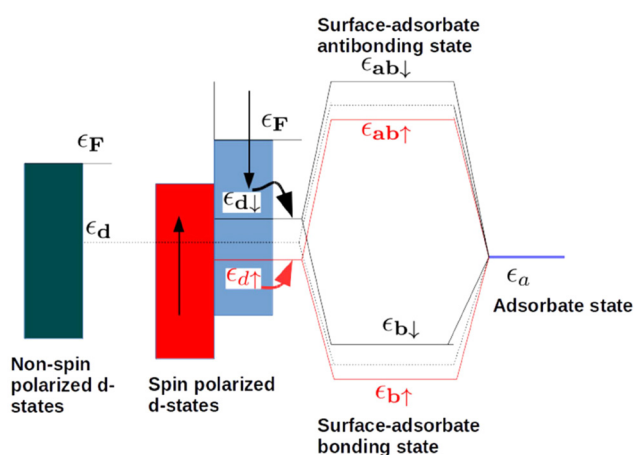


Fig. 16 Schematic illustration of the coupling of an adsorbate level ϵ_a with the metal d -states characterized by a single d -band center (non-spin-polarized case, ϵ_d , dotted line) and two d -band centers, and $\epsilon_{d\uparrow}$ and $\epsilon_{d\downarrow}$ for the spin-polarized case.¹²¹ Reproduced from ref. 121 with permission from Springer Nature, copyright 2016.

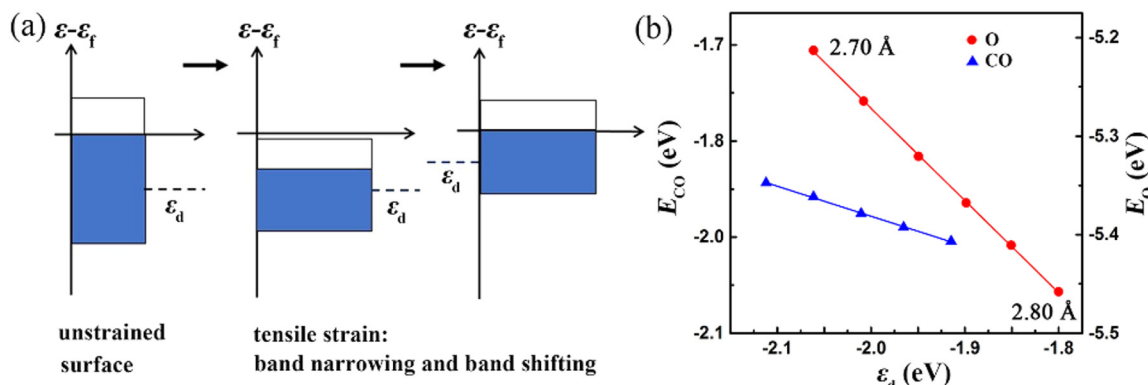


Fig. 17 The electronic properties of strain effects. (a) The illustration of the effect of tensile strain on the d -band of transition metals (TMs). (b) The adsorption energies of CO and O under strain *versus* the d -band center ϵ_d on Ru (0001) surface.²⁰⁰ Reproduced from ref. 200 with permission from the American Physical Society, copyright 1998.

lyst could be modified to induce a downward shift of the d -band.

As a component of the electronic system of the catalyst, the shift of the d -band center is altered not only by changes in composition,^{174–177} but also by defects,^{157,178,179} the strain effect^{180–183} and phase transitions.¹⁸⁴ There is therefore no need to invent entirely new catalysts with higher efficiencies than current ones. Rather we can improve them by alloying,¹⁸⁵ doping,^{186–188} or strain engineering.^{189–191} In addition, changing the support material¹⁹² or the neighboring atoms of the single atom catalyst¹⁹³ can also lead to a d -band shift and thus to a change in catalytic activity. Different core–shell structures result from the re-engineering of existing nanosized catalysts.^{167–170}

It is worth noting that there are correlations between the position of the d -band and the adsorption strength, as well as the position of the given transition metal in the periodic table. As the number of electrons on the outer shell of the transition metal increases, the number of anti-bonding states in the d -band likewise increases. Consequently, the attractive interactions are weaker towards the right side of the periodic table. Au can therefore be considered as the noblest metal.¹³⁸ Clearly, as the group number increases, the values of ϵ_d and W_d decrease for the later transition metals. However, for the early transition metals, ϵ_d and W_d show different trends with group number. There are some anomalies in this correlation for Ni, Pd and Pt. Consequently, the d -band center model proves ineffective in predicting the catalytic activity of near-surface alloys with Pt skin.¹¹⁹

Furthermore, the d -band model is inadequate for molecules with a strong dipole moment. This is due to the fact that the d -band center model predicts a consistent decrease or increase in the adsorption energy of a given molecule from one TM surface to another without taking into account the spin polarization of an adsorbate. Therefore, exceptions usually occur when the adsorbate has a high electronegativity and the substrate has an almost full d -band. And one of the notable exceptions is the adsorption of OH on Pt and Pd skin alloy systems.¹⁹⁴

Charge density

Since the adsorption and catalytic processes involve charge transfer from the adsorbate to the catalyst surface, they can be described in terms of surface charge density. Many molecules have an intrinsic charge redistribution, known as a dipole moment, due to differences in electronegativity between atoms in the molecule. For example, in SO_2 ¹⁹⁵ and CO ¹⁹⁶ molecules, the oxygen atom gains electrons from the carbon atom, resulting in a dipole moment. The surface charge therefore has a significant effect on the adsorption process. Charge redistribution on the surface can be computed by calculating the Bader charges,¹⁹⁷ which represent the interaction between atoms and the positions of the highest localizations of electronic density.

Adsorption and catalytic processes require additional electrons, so a negatively charged surface is preferred. For example, the CO_2 molecule always gains some electrons from the surface¹⁹⁸ and is therefore difficult to adsorb on an electron-deficient surface. In contrast, some molecules such as CO ^{85,86} and O_2 ¹⁹⁹ prefer to adsorb on positively charged surfaces. Calculations of charge density and its redistribution on the surface therefore allow the active adsorption sites for a particular molecule to be identified.

Strain effect

Strains of various types can be observed in the metal alloys and ultrathin coatings.^{182,190,200–202} Such strains occur due to differences in the lattice parameters of the metals used in the alloy or in the core–shell particles. The introduction of strain into the crystal lattices of the electrocatalyst significantly perturbs its electronic structure. This results in increased electrocatalytic activity through the strain–adsorption–reactivity relationship.^{201,203} Tensile stretching or compression of the surface results in an increase or decrease in atomic spacing, leading to a decrease or increase in orbital overlap.²⁰⁴ Therefore, descriptors based on the electronic structures of the catalyst could be used for consideration. As the strain affects

the geometry and electronic structure of the catalyst its description could be achieved by using the orbitalwise coordination number^{120,205} in the following way:

$$\overline{\text{CN}}^*(i) = \frac{1}{1+S} \overline{\text{CN}}(i)$$

where S is the strain coefficient, which is negative for a compression and positive for a tension. This simple modification allows us to account for changes in the strength of the interaction between atoms under strain.

The application of strain induces changes in the electronic structure, resulting in charge redistribution and a d -band shift.^{100,201} Compressive strain causes a downshift of the d -band, whereas tensile strain causes an upshift, as shown in Fig. 17a. Therefore, the change in catalytic properties of the core–shell structures^{167–170} compared with the pure metals²⁰⁶ can be attributed to the d -band shift of the core metal. This provides an excellent opportunity to tune the catalytic properties of the material using the d -band center model.

From compressive strain to tensile strain, the d -band shifts to a higher energy position, increasing the probability of the anti-bonding states coupled by the adsorbate and metal d -states being pushed above the Fermi level. Consequently, greater strain results in a stronger net attractive interaction and a higher adsorption energy.¹⁰⁰ As the shift of the d -band is aptly described by the center of ϵ_d , the d -band center model is a suitable descriptor to illustrate strain trends. The changes in adsorption energies during strain are shown in Fig. 17b.

Conclusions

Core–shell nanostructures have unique properties that have stimulated considerable research and offer considerable potential for the design of finely tuned nanocatalysts with desired activity and selectivity. The successful synthesis, study and application of core–shell nanostructures in catalysis requires attention to a number of critical areas.

Firstly, the problem of determining the surface composition of core–shell nanostructures hinders a new understanding of the relationship between their structure and properties. In order to achieve the rational synthesis of bimetallic core–shell nanostructures, the elucidation of their surface composition and dynamic changes is essential for the successful development of this field. Due to the excessive depth of electron penetration, some electron microscopic and spectroscopic methods perform poorly in this direction. In contrast, many probe-based methods appear to be powerful tools for solving these problems. In particular, techniques such as ET, STM, SERS and IR hold great promise for revealing the surface properties of bimetallic core–shell nanostructures.²⁰⁷ However, all four tools have drawbacks to varying degrees.

Secondly, there is a need to develop theoretical methods for the study of nanomaterials. An important advantage of this approach is the ability to predict the properties of compounds that have not yet been studied experimentally, and whose syn-

thesis and analysis can be a material and time-consuming task. To understand the potential prospects of using nanostructures in catalysis, it is necessary to propose and derive an efficient and accurate descriptor to describe the catalytic properties of such complex objects, since it is not only the nearest neighbors that determine the catalytic properties of active sites. The most effective way to obtain a new descriptor is to use modern developments in the field of artificial intelligence, including graph neural networks, which allow the atomic structure of a nanoparticle to be deciphered to reveal structure–property relationships.

Thirdly, a review of the numerous studies on metallic and bimetallic nanoparticles highlights the importance of synergistic effects in optimizing catalytic properties. This effect can potentially be enhanced when considering more complex systems such as high-entropy alloys. Several papers have been devoted to the realization of experimental techniques for the synthesis of such complex alloys consisting of 11–21 metals.^{208–211} Prior to the application of these materials in catalysis, it is necessary to carry out the identification of the properties that are mainly responsible for the optimization of the catalytic properties for a given reaction. Recently, the hydrogen evolution reaction has been tested on such objects,^{212,213} indicating great prospects for the use of high-entropy alloy nanoparticles in this reaction. However, the use of HEA NPs is still controversial as the methods for optimization of their structure and properties need to be improved.²¹⁴ Experimental techniques allow the synthesis of high-entropy carbides in the form of nanometer-sized particles.^{215,216} The atomic structure of such nanoparticles is even more complex than that of HEAs containing metallic and non-metallic atoms that influence the catalytic activity of the active sites. The consideration of carbides can also be extended to borides. High-entropy borides are now also being considered as alternative materials for catalytic reactions.^{217,218}

Author contributions

I. V. C. – conceptualization; I. V. C., A. D. R. – data curation; A. G. K. – supervision; I. V. C., A. D. R., A. G. K. – writing – original draft; I. V. C., A. D. R., A. G. K. – writing – review & editing.

Conflicts of interest

There are no conflicts to declare.

References

- 1 L. Liu and A. Corma, *Chem. Rev.*, 2023, **123**, 4855–4933.
- 2 Y. Nakaya and S. Furukawa, *Chem. Rev.*, 2023, **123**, 5859–5947.
- 3 F. Zaera, *Chem. Rev.*, 2022, **122**, 8594–8757.
- 4 Y. Guo, M. Wang, Q. Zhu, D. Xiao and D. Ma, *Nat. Catal.*, 2022, **5**, 766–776.

- 5 K. M. Neyman and S. M. Kozlov, *NPG Asia Mater.*, 2022, **14**, 1–8.
- 6 P. C. D. Mendes, Y. Song, W. Ma, T. Z. H. Gani, K. H. Lim, S. Kawi and S. M. Kozlov, *Adv. Phys.: X*, 2023, **8**, 2175623.
- 7 D. Leybo, K. L. Firestein, N. D. Evdokimenko, A. A. Ryzhova, V. S. Baidyshev, I. V. Chepkasov, Z. I. Popov, A. L. Kustov, A. S. Konopatsky, D. V. Golberg and D. V. Shtansky, *ACS Appl. Nano Mater.*, 2022, **5**, 16475–16488.
- 8 A. M. Kovalskii, I. N. Volkov, N. D. Evdokimenko, O. P. Tkachenko, D. V. Leybo, I. V. Chepkasov, Z. I. Popov, A. T. Matveev, A. Manakhov, E. S. Permyakova, A. S. Konopatsky, A. L. Kustov, D. V. Golberg and D. V. Shtansky, *Appl. Catal., B*, 2022, **303**, 120891.
- 9 A. S. Konopatsky, K. L. Firestein, N. D. Evdokimenko, A. L. Kustov, V. S. Baidyshev, I. V. Chepkasov, Z. I. Popov, A. T. Matveev, I. V. Shetinin, D. V. Leybo, I. N. Volkov, A. M. Kovalskii, D. Golberg and D. V. Shtansky, *J. Catal.*, 2021, **402**, 130–142.
- 10 A. S. Konopatsky, D. V. Leybo, K. L. Firestein, I. V. Chepkasov, Z. I. Popov, E. S. Permyakova, I. N. Volkov, A. M. Kovalskii, A. T. Matveev, D. V. Shtansky and D. V. Golberg, *ChemCatChem*, 2020, **12**, 1691–1698.
- 11 V. A. Ponomarev, A. N. Sheveyko, E. S. Permyakova, J. Lee, A. A. Voevodin, D. Berman, A. M. Manakhov, M. Michlíček, P. V. Slukin, V. V. Firstova, S. G. Ignatov, I. V. Chepkasov, Z. I. Popov and D. V. Shtansky, *ACS Appl. Mater. Interfaces*, 2019, **11**, 28699–28719.
- 12 I. V. Chepkasov, Yu. Ya. Gafner and S. L. Gafner, *J. Aerosol Sci.*, 2016, **91**, 33–42.
- 13 Yu. Ya. Gafner, S. L. Gafner and I. V. Chepkasov, *J. Exp. Theor. Phys.*, 2010, **111**, 608–618.
- 14 N. V. Suetin, S. A. Evlashin, A. V. Egorov, K. V. Mironovich, S. A. Dagesyan, L. V. Yashina, E. A. Goodilin and V. A. Krivchenko, *Phys. Chem. Chem. Phys.*, 2016, **18**, 12344–12349.
- 15 B. I. Podlovchenko, V. A. Krivchenko, Yu. M. Maksimov, T. D. Gladysheva, L. V. Yashina, S. A. Evlashin and A. A. Pilevsky, *Electrochim. Acta*, 2012, **76**, 137–144.
- 16 I. V. Chepkasov, Yu. Ya. Gafner and S. L. Gafner, *Phase Transitions*, 2017, **90**, 590–597.
- 17 R. Ferrando, J. Jellinek and R. L. Johnston, *Chem. Rev.*, 2008, **108**, 845–910.
- 18 D. Astruc, *Chem. Rev.*, 2020, **120**, 461–463.
- 19 W. Li, K. Liu, S. Feng, Y. Xiao, L. Zhang, J. Mao, Q. Liu, X. Liu, J. Luo and L. Han, *J. Colloid Interface Sci.*, 2024, **655**, 726–735.
- 20 M. Yang, T. Wei, J. He, Q. Liu, L. Feng, H. Li, J. Luo and X. Liu, *Nano Res.*, 2024, **17**, 1209–1216.
- 21 T. Wang, Q. Zhang, K. Lian, G. Qi, Q. Liu, L. Feng, G. Hu, J. Luo and X. Liu, *J. Colloid Interface Sci.*, 2024, **655**, 176–186.
- 22 Y. M. Maksimov, B. I. Podlovchenko, E. M. Gallyamov, S. A. Dagesyan, V. V. Sen and S. A. Evlashin, *Mendeleev Commun.*, 2017, **27**, 382–384.
- 23 B. I. Podlovchenko, Yu. M. Maksimov, S. A. Evlashin, T. D. Gladysheva, K. I. Maslakov and V. A. Krivchenko, *J. Electroanal. Chem.*, 2015, **743**, 93–98.
- 24 B. I. Podlovchenko, Yu. M. Maksimov, D. S. Volkov and S. A. Evlashin, *J. Electroanal. Chem.*, 2020, **858**, 113787.
- 25 M. Haruta, T. Kobayashi, H. Sano and N. Yamada, *Chem. Lett.*, 1987, **16**, 405–408.
- 26 H. S. Zhou, H. Sasahara, I. Honma, H. Komiyama and J. W. Haus, *Chem. Mater.*, 1994, **6**, 1534–1541.
- 27 C. F. Hoener, K. A. Allan, A. J. Bard, A. Campion, M. A. Fox, T. E. Mallouk, S. E. Webber and J. M. White, *J. Phys. Chem.*, 1992, **96**, 3812–3817.
- 28 I. Honma, T. Sano and H. Komiyama, *J. Phys. Chem.*, 1993, **97**, 6692–6695.
- 29 Q. Zhang, I. Lee, J. B. Joo, F. Zaera and Y. Yin, *Acc. Chem. Res.*, 2013, **46**, 1816–1824.
- 30 R. Ghosh Chaudhuri and S. Paria, *Chem. Rev.*, 2012, **112**, 2373–2433.
- 31 X. Cui, A. P. van Muyden and P. J. Dyson, *Chem. – Eur. J.*, 2021, **27**, 12–19.
- 32 S. Das, J. Pérez-Ramírez, J. Gong, N. Dewangan, K. Hidajat, B. C. Gates and S. Kawi, *Chem. Soc. Rev.*, 2020, **49**, 2937–3004.
- 33 C. Wang, Y. Shi, D. Qin and Y. Xia, *Nanoscale Horiz.*, 2023, **8**, 1194–1204.
- 34 J. E. S. van der Hoeven, J. Jelic, L. A. Olthof, G. Totarella, R. J. A. van Dijk-Moes, J.-M. Krafft, C. Louis, F. Studt, A. van Blaaderen and P. E. de Jongh, *Nat. Mater.*, 2021, **20**, 1216–1220.
- 35 M. Luo and S. Guo, *Nat. Rev. Mater.*, 2017, **2**, 1–13.
- 36 A. K. Singh and Q. Xu, *ChemCatChem*, 2013, **5**, 652–676.
- 37 X. Wang, S.-I. Choi, L. T. Roling, M. Luo, C. Ma, L. Zhang, M. Chi, J. Liu, Z. Xie, J. A. Herron, M. Mavrikakis and Y. Xia, *Nat. Commun.*, 2015, **6**, 7594.
- 38 M. B. Gawande, A. Goswami, T. Asefa, H. Guo, A. V. Biradar, D.-L. Peng, R. Zboril and R. S. Varma, *Chem. Soc. Rev.*, 2015, **44**, 7540–7590.
- 39 T. He, W. Wang, F. Shi, X. Yang, X. Li, J. Wu, Y. Yin and M. Jin, *Nature*, 2021, **598**, 76–81.
- 40 P. Strasser, S. Koh, T. Anniyev, J. Greeley, K. More, C. Yu, Z. Liu, S. Kaya, D. Nordlund, H. Ogasawara, M. F. Toney and A. Nilsson, *Nat. Chem.*, 2010, **2**, 454–460.
- 41 J. A. Rodriguez, *Surf. Sci. Rep.*, 1996, **24**, 223–287.
- 42 M. Mavrikakis, B. Hammer and J. K. Nørskov, *Phys. Rev. Lett.*, 1998, **81**, 2819–2822.
- 43 L. A. Kibler, A. M. El-Aziz, R. Hoyer and D. M. Kolb, *Angew. Chem., Int. Ed.*, 2005, **44**, 2080–2084.
- 44 X. Yang, Y. Wang, X. Tong and N. Yang, *Adv. Energy Mater.*, 2022, **12**, 2102261.
- 45 X. Mao, Z. Qin, S. Ge, C. Rong, B. Zhang and F. Xuan, *Mater. Horiz.*, 2023, **10**, 340–360.
- 46 S. U. Son, Y. Jang, J. Park, H. B. Na, H. M. Park, H. J. Yun, J. Lee and T. Hyeon, *J. Am. Chem. Soc.*, 2004, **126**, 5026–5027.
- 47 X. Zhang, S. Han, B. Zhu, G. Zhang, X. Li, Y. Gao, Z. Wu, B. Yang, Y. Liu, W. Baaziz, O. Ersen, M. Gu, J. T. Miller and W. Liu, *Nat. Catal.*, 2020, **3**, 411–417.

- 48 P. Grammatikopoulos, S. Steinhauer, J. Vernieres, V. Singh and M. Sowwan, *Adv. Phys.: X*, 2016, **1**, 81–100.
- 49 T. V. Pfeiffer, P. Kedia, M. E. Messing, M. Valvo and A. Schmidt-Ott, *Materials*, 2015, **8**, 1027–1042.
- 50 N. Eom, M. E. Messing, J. Johansson and K. Deppert, *ACS Nano*, 2021, **15**, 8883–8895.
- 51 K. D. Gilroy, A. Ruditskiy, H.-C. Peng, D. Qin and Y. Xia, *Chem. Rev.*, 2016, **116**, 10414–10472.
- 52 M. Ahmadi, F. Behafarid, C. Cui, P. Strasser and B. R. Cuenya, *ACS Nano*, 2013, **7**, 9195–9204.
- 53 C. J. Serpell, J. Cookson, D. Ozkaya and P. D. Beer, *Nat. Chem.*, 2011, **3**, 478–483.
- 54 J. Zhang, M. B. Vukmirovic, Y. Xu, M. Mavrikakis and R. R. Adzic, *Angew. Chem., Int. Ed.*, 2005, **44**, 2132–2135.
- 55 D. Nelli, C. Roncaglia and C. Minnai, *Adv. Phys.: X*, 2023, **8**, 2127330.
- 56 D. Nelli, C. Roncaglia, R. Ferrando and C. Minnai, *J. Phys. Chem. Lett.*, 2021, **12**, 4609–4615.
- 57 R. Lamber, S. Wetjen and N. I. Jaeger, *Phys. Rev. B: Condens. Matter Mater. Phys.*, 1995, **51**, 10968–10971.
- 58 D. Nafday, S. Sarkar, P. Ayub and T. Saha-Dasgupta, *ACS Nano*, 2018, **12**, 7246–7252.
- 59 C. Solliard and M. Flueli, *Surf. Sci.*, 1985, **156**, 487–494.
- 60 Y. Lei, J. Jelic, L. C. Nitsche, R. Meyer and J. Miller, *Top. Catal.*, 2011, **54**, 334–348.
- 61 N. Weiher, E. Bus, L. Delannoy, C. Louis, D. E. Ramaker, J. T. Miller and J. A. van Bokhoven, *J. Catal.*, 2006, **240**, 100–107.
- 62 I. V. Chepkasov, M. A. Visotin, E. A. Kovaleva, A. M. Manakhov, V. S. Baidyshev and Z. I. Popov, *J. Phys. Chem. C*, 2018, **122**, 18070–18076.
- 63 X. Zhang, Z. Sun, R. Jin, C. Zhu, C. Zhao, Y. Lin, Q. Guan, L. Cao, H. Wang, S. Li, H. Yu, X. Liu, L. Wang, S. Wei, W.-X. Li and J. Lu, *Nat. Commun.*, 2023, **14**, 530.
- 64 Q. Guan, C. Zhu, Y. Lin, E. I. Vovk, X. Zhou, Y. Yang, H. Yu, L. Cao, H. Wang, X. Zhang, X. Liu, M. Zhang, S. Wei, W.-X. Li and J. Lu, *Nat. Catal.*, 2021, **4**, 840–849.
- 65 A. Wang, X. Y. Liu, C.-Y. Mou and T. Zhang, *J. Catal.*, 2013, **308**, 258–271.
- 66 J. Shi, *Chem. Rev.*, 2013, **113**, 2139–2181.
- 67 N. M. Marković and P. N. Ross, *Surf. Sci. Rep.*, 2002, **45**, 117–229.
- 68 M. F. Francis and W. A. Curtin, *Nat. Commun.*, 2015, **6**, 6261.
- 69 W. An and P. Liu, *J. Phys. Chem. C*, 2013, **117**, 16144–16149.
- 70 I. E. L. Stephens, A. S. Bondarenko, U. Grønbjerg, J. Rossmeisl and I. Chorkendorff, *Energy Environ. Sci.*, 2012, **5**, 6744–6762.
- 71 J. A. Herron, J. Jiao, K. Hahn, G. Peng, R. R. Adzic and M. Mavrikakis, *Electrocatalysis*, 2012, **3**, 192–202.
- 72 J. Wu, L. Qi, H. You, A. Gross, J. Li and H. Yang, *J. Am. Chem. Soc.*, 2012, **134**, 11880–11883.
- 73 I. V. Chepkasov, V. S. Baidyshev, A. A. Golubnichiy, I. S. Zamulin, A. G. Kvashnin and S. M. Kozlov, *Aggregate*, 2022, **3**, e273.
- 74 X.-N. Li, Z. Yuan and S.-G. He, *J. Am. Chem. Soc.*, 2014, **136**, 3617–3623.
- 75 J.-J. Chen, X.-N. Li, Q. Chen, Q.-Y. Liu, L.-X. Jiang and S.-G. He, *J. Am. Chem. Soc.*, 2019, **141**(5), 2027–2034.
- 76 A. Patra, J. E. Bates, J. Sun and J. P. Perdew, *Proc. Natl. Acad. Sci. U. S. A.*, 2017, **114**, E9188–E9196.
- 77 J. Wu, S. Shan, H. Cronk, F. Chang, H. Kareem, Y. Zhao, J. Luo, V. Petkov and C.-J. Zhong, *J. Phys. Chem. C*, 2017, **121**, 14128–14136.
- 78 T. Ishimoto and M. Koyama, *J. Phys. Chem. Lett.*, 2016, **7**, 736–740.
- 79 Y. Liang, C. Ou, H. Zhang, X. Ding, M. Zhao, J. Wang and Y. Chen, *Ind. Eng. Chem. Res.*, 2018, **57**, 3887–3897.
- 80 J. Wang, D. Liu, L. Li, X. Qi, K. Xiong, W. Ding, S. Chen and Z. Wei, *J. Phys. Chem. C*, 2017, **121**, 8781–8786.
- 81 J. X. Wang, H. Inada, L. Wu, Y. Zhu, Y. Choi, P. Liu, W.-P. Zhou and R. R. Adzic, *J. Am. Chem. Soc.*, 2009, **131**, 17298–17302.
- 82 I. V. Chepkasov, V. S. Baidyshev and A. G. Kvashnin, *Phys. Rev. B*, 2023, **108**, 205414.
- 83 S. Jiao, X. Fu and H. Huang, *Adv. Funct. Mater.*, 2022, **32**, 2107651.
- 84 I. V. Chepkasov, I. S. Zamulin, V. S. Baidyshev and A. G. Kvashnin, *Phys. Chem. Chem. Phys.*, 2023, **25**, 33031–33037.
- 85 X.-N. Li, Z. Yuan and S.-G. He, *J. Am. Chem. Soc.*, 2014, **136**, 3617–3623.
- 86 J.-J. Chen, X.-N. Li, Q. Chen, Q.-Y. Liu, L.-X. Jiang and S.-G. He, *J. Am. Chem. Soc.*, 2019, **141**, 2027–2034.
- 87 W.-Y. Yu, G. M. Mullen and C. B. Mullins, *J. Phys. Chem. C*, 2013, **117**, 19535–19543.
- 88 Á. Molnár, A. Sárkány and M. Varga, *J. Mol. Catal. A: Chem.*, 2001, **173**, 185–221.
- 89 J. Silvestre-Albero, G. Rupprechter and H.-J. Freund, *Chem. Commun.*, 2006, 80–82.
- 90 B. Bachiller-Baeza, A. Iglesias-Juez, E. Castillejos-López, A. Guerrero-Ruiz, M. D. Michiel, M. Fernández-García and I. Rodríguez-Ramos, *ACS Catal.*, 2015, **5**, 5235–5241.
- 91 A. Hugon, L. Delannoy, J.-M. Krafft and C. Louis, *J. Phys. Chem. C*, 2010, **114**, 10823–10835.
- 92 N. E. Kolli, L. Delannoy and C. Louis, *J. Catal.*, 2013, **297**, 79–92.
- 93 B. Goris, S. Bals, W. Van den Broek, E. Carbó-Argibay, S. Gómez-Graña, L. M. Liz-Marzán and G. Van Tendeloo, *Nat. Mater.*, 2012, **11**, 930–935.
- 94 S. Xie, S.-I. Choi, N. Lu, L. T. Roling, J. A. Herron, L. Zhang, J. Park, J. Wang, M. J. Kim, Z. Xie, M. Mavrikakis and Y. Xia, *Nano Lett.*, 2014, **14**, 3570–3576.
- 95 H. Tianou, W. Wang, X. Yang, Z. Cao, Q. Kuang, Z. Wang, Z. Shan, M. Jin and Y. Yin, *Nat. Commun.*, 2017, **8**, 1261.
- 96 J. Zhu, Z. Lyu, Z. Chen, M. Xie, M. Chi, W. Jin and Y. Xia, *Chem. Mater.*, 2019, **31**, 5867–5875.
- 97 T. Reier, M. Oezaslan and P. Strasser, *ACS Catal.*, 2012, **2**, 1765–1772.
- 98 S. Park, Y. Shao, J. Liu and Y. Wang, *Energy Environ. Sci.*, 2012, **5**, 9331–9344.

- 99 E. Antolini, *ACS Catal.*, 2014, **4**, 1426–1440.
- 100 B. Li, W. Gao and Q. Jiang, *J. Phys. Energy*, 2021, **3**, 022001.
- 101 S. Piccinin and M. Stamatakis, *ACS Catal.*, 2014, **4**, 2143–2152.
- 102 K. J. Laidler, *Pure Appl. Chem.*, 1996, **68**, 149–192.
- 103 Z. Duan and G. Henkelman, *ACS Catal.*, 2014, **4**, 3435–3443.
- 104 N. K. Soliman, *J. Mater. Res. Technol.*, 2019, **8**, 2395–2407.
- 105 C. Feng, X. Liu, T. Zhu and M. Tian, *Environ. Sci. Pollut. Res.*, 2021, 24847–24871.
- 106 G. Kresse and J. Furthmüller, *Phys. Rev. B: Condens. Matter Mater. Phys.*, 1996, **16**, 11169–11186.
- 107 G. Kresse and J. Furthmüller, *Comput. Mater. Sci.*, 1996, **6**, 15–50.
- 108 R. Nelson, C. Ertural, J. George, V. L. Deringer, G. Hautier and R. Dronskowski, *J. Comput. Chem.*, 2020, **41**, 1931–1940.
- 109 P. Giannozzi, S. Baroni, N. Bonini, M. Calandra, R. Car, C. Cavazzoni, D. Ceresoli, G. L. Chiarotti, M. Cococcioni and I. Dabo, *J. Phys.: Condens. Matter*, 2009, **21**, 395502.
- 110 P. Giannozzi, O. Andreussi, T. Brumme, O. Bunau, M. B. Nardelli, M. Calandra, R. Car, C. Cavazzoni, D. Ceresoli, M. Cococcioni, N. Colonna, I. Carnimeo, A. D. Corso, S. de Gironcoli, P. Delugas, R. A. DiStasio, A. Ferretti, A. Floris, G. Fratesi, G. Fugallo, R. Gebauer, U. Gerstmann, F. Giustino, T. Gorni, J. Jia, M. Kawamura, H.-Y. Ko, A. Kokalj, E. Küçükbenli, M. Lazzeri, M. Marsili, N. Marzari, F. Mauri, N. L. Nguyen, H.-V. Nguyen, A. Otero-de-la-Roza, L. Paulatto, S. Poncé, D. Rocca, R. Sabatini, B. Santra, M. Schlipf, A. P. Seitsonen, A. Smogunov, I. Timrov, T. Thonhauser, P. Umari, N. Vast, X. Wu and S. Baroni, *J. Phys.: Condens. Matter*, 2017, **29**, 465901.
- 111 X. Gonze, B. Amadon, P.-M. Anglade, J.-M. Beuken, F. Bottin, P. Boulanger, F. Bruneval, D. Caliste, R. Caracas, M. Côté, T. Deutsch, L. Genovese, Ph. Ghosez, M. Giantomassi, S. Goedecker, D. R. Hamann, P. Hermet, F. Jollet, G. Jomard, S. Leroux, M. Mancini, S. Mazevedt, M. J. T. Oliveira, G. Onida, Y. Pouillon, T. Rangel, G.-M. Rignanese, D. Sangalli, R. Shaltaf, M. Torrent, M. J. Verstraete, G. Zerah and J. W. Zwanziger, *Comput. Phys. Commun.*, 2009, **180**, 2582–2615.
- 112 A. Chen, X. Zhang, L. Chen, S. Yao and Z. Zhou, *J. Phys. Chem. C*, 2020, **124**, 22471–22478.
- 113 M. Zhong, K. Tran, Y. Min, C. Wang, Z. Wang, C.-T. Dinh, P. De Luna, Z. Yu, A. S. Rasouli, P. Brodersen, S. Sun, O. Voznyy, C.-S. Tan, M. Askerka, F. Che, M. Liu, A. Seifitokaldani, Y. Pang, S.-C. Lo, A. Ip, Z. Ulissi and E. H. Sargent, *Nature*, 2020, **581**, 178–183.
- 114 K. Tran and Z. W. Ulissi, *Nat. Catal.*, 2018, **1**, 696–703.
- 115 Z. Li, S. Wang, W. S. Chin, L. E. Achenie and H. Xin, *J. Mater. Chem. A*, 2017, **5**, 24131–24138.
- 116 X. Ma and H. Xin, *Phys. Rev. Lett.*, 2017, **118**, 036101.
- 117 N. C. Frey, D. Akinwande, D. Jariwala and V. B. Shenoy, *ACS Nano*, 2020, **14**, 13406–13417.
- 118 D. Wu, J. Zhang, M.-J. Cheng, Q. Lu and H. Zhang, *J. Phys. Chem. C*, 2021, **125**, 15363–15372.
- 119 F. Calle-Vallejo, J. I. Martínez, J. M. García-Lastra, P. Sautet and D. Loffreda, *Angew. Chem., Int. Ed.*, 2014, **53**, 8316–8319.
- 120 F. Calle-Vallejo, *Adv. Sci.*, 2023, **10**, 2207644.
- 121 S. Bhattacharjee, U. V. Waghmare and S.-C. Lee, *Sci. Rep.*, 2016, **6**, 35916.
- 122 X. Wan, Z. Zhang, H. Niu, Y. Yin, C. Kuai, J. Wang, C. Shao and Y. Guo, *J. Phys. Chem. Lett.*, 2021, **12**, 6111–6118.
- 123 Y.-L. Wang, Y. Tian, Z.-L. Lang, W. Guan and L.-K. Yan, *J. Mater. Chem. A*, 2018, **6**, 21056–21063.
- 124 P. Li, H. Hu, G. Luo, S. Zhu, L. Guo, P. Qu, Q. Shen and T. He, *ACS Appl. Mater. Interfaces*, 2020, **12**, 56039–56048.
- 125 Y. Wang, Y. Tian, L. Yan and Z. Su, *J. Phys. Chem. C*, 2018, **122**, 7712–7719.
- 126 X. Ma, Z. Li, L. E. K. Achenie and H. Xin, *J. Phys. Chem. Lett.*, 2015, **6**, 3528–3533.
- 127 Y. Xiao and W. Zhang, *Nanoscale*, 2020, **12**, 7660–7673.
- 128 T. Shen, Z. Wang, S.-M. Xu, X. Sun, G. Liu, S. Bai, J. Li, Z. Song, L. Zheng and Y.-F. Song, *Cell Rep. Phys. Sci.*, 2023, 101478.
- 129 R. Long, Y. Li, Y. Liu, S. Chen, X. Zheng, C. Gao, C. He, N. Chen, Z. Qi, L. Song, J. Jiang, J. Zhu and Y. Xiong, *J. Am. Chem. Soc.*, 2017, **139**, 4486–4492.
- 130 B. Garlyyev, J. Fichtner, O. Piqué, O. Schneider, A. S. Bandarenka and F. Calle-Vallejo, *Chem. Sci.*, 2019, **10**, 8060–8075.
- 131 A. S. Bazhenov, L. Lefferts and K. Honkala, *J. Phys. Chem. C*, 2017, **121**, 4324–4331.
- 132 Z. Zhao, Z. Chen, X. Zhang and G. Lu, *J. Phys. Chem. C*, 2016, **120**(49), 28125–28130.
- 133 S. Hanselman, M. T. M. Koper and F. Calle-Vallejo, *Phys. Chem. Chem. Phys.*, 2023, **25**, 3211–3219.
- 134 S. D. Miller, N. İnoğlu and J. R. Kitchin, *J. Chem. Phys.*, 2011, **134**, 104709.
- 135 Y. Nanba and M. Koyama, *ACS Omega*, 2021, **6**, 3218–3226.
- 136 J. P. Gaspard and F. Cyrot-Lackmann, *J. Phys. C: Solid State Phys.*, 1973, **6**, 3077.
- 137 B. Hammer and J. K. Nørskov, *Surf. Sci.*, 1995, **343**, 211–220.
- 138 B. Hammer and J. K. Nørskov, *Nature*, 1995, **376**, 238–240.
- 139 B. Hammer and J. K. Nørskov, in *Advances in Catalysis*, Academic Press, 2000, vol. 45, pp. 71–129.
- 140 Q. Jiang, H. M. Lu and M. Zhao, *J. Phys.: Condens. Matter*, 2004, **16**, 521.
- 141 M. Methfessel, D. Hennig and M. Scheffler, *Phys. Rev. B: Condens. Matter Mater. Phys.*, 1992, **46**, 4816–4829.
- 142 B. Hammer, O. H. Nielsen and J. K. Nørskov, *Catal. Lett.*, 1997, **46**, 31–35.
- 143 P. Kratzer, B. Hammer and J. K. Nørskov, *Surf. Sci.*, 1996, **359**, 45–53.
- 144 P. W. Anderson, *Phys. Rev.*, 1961, **124**, 41–53.
- 145 D. M. Newns, *Phys. Rev.*, 1969, **178**, 1123–1135.
- 146 T. Gunji, R. H. Wakabayashi, S. H. Noh, B. Han, F. Matsumoto, F. J. DiSalvo and H. D. Abruna, *Electrochim. Acta*, 2018, **283**, 1045–1052.

- 147 W. Zhang, C. Xu, Y. Hu, S. Yang, L. Ma, L. Wang, P. Zhao, C. Wang, J. Ma and Z. Jin, *Nano Energy*, 2020, **73**, 104796.
- 148 X. Zhu, Q. Guo, Y. Sun, S. Chen, J.-Q. Wang, M. Wu, W. Fu, Y. Tang, X. Duan, D. Chen and Y. Wan, *Nat. Commun.*, 2019, **10**, 1428.
- 149 W. Zhang, Q. Yao, G. Jiang, C. Li, Y. Fu, X. Wang, A. Yu and Z. Chen, *ACS Catal.*, 2019, **9**, 11603–11613.
- 150 Y. Chen, J. Cai, P. Li, G. Zhao, G. Wang, Y. Jiang, J. Chen, S. X. Dou, H. Pan and W. Sun, *Nano Lett.*, 2020, **20**, 6807–6814.
- 151 G. Shen, R. Zhang, L. Pan, F. Hou, Y. Zhao, Z. Shen, W. Mi, C. Shi, Q. Wang, X. Zhang and J.-J. Zou, *Angew. Chem., Int. Ed.*, 2020, **59**, 2313–2317.
- 152 H. Yang, Y. Hu, J. Chen, M.-Sadeeq Balogun, P. Fang, S. Zhang, J. Chen and Y. Tong, *Adv. Energy Mater.*, 2019, **9**, 1901396.
- 153 L. Wang, Z. Li, K. Wang, Q. Dai, C. Lei, B. Yang, Q. Zhang, L. Lei, M. K. H. Leung and Y. Hou, *Nano Energy*, 2020, **74**, 104850.
- 154 M. Retuerto, L. Pascual, F. Calle-Vallejo, P. Ferrer, D. Gianolio, A. G. Pereira, Á. García, J. Torrero, M. T. Fernández-Díaz, P. Bencok, M. A. Peña, J. L. G. Fierro and S. Rojas, *Nat. Commun.*, 2019, **10**, 2041.
- 155 M. Cho, J. T. Song, S. Back, Y. Jung and J. Oh, *ACS Catal.*, 2018, **8**, 1178–1185.
- 156 Q. Li, X. Zou, X. Ai, H. Chen, L. Sun and X. Zou, *Adv. Energy Mater.*, 2019, **9**, 1803369.
- 157 Y. Wu, J. Cai, Y. Xie, S. Niu, Y. Zang, S. Wu, Y. Liu, Z. Lu, Y. Fang, Y. Guan, X. Zheng, J. Zhu, X. Liu, G. Wang and Y. Qian, *Adv. Mater.*, 2020, **32**, 1904346.
- 158 J. Xu, Z. Lian, B. Wei, Y. Li, O. Bondarchuk, N. Zhang, Z. Yu, A. Araujo, I. Amorim, Z. Wang, B. Li and L. Liu, *ACS Catal.*, 2020, **10**, 3571–3579.
- 159 L. Xiong, Z. Sun, X. Zhang, L. Zhao, P. Huang, X. Chen, H. Jin, H. Sun, Y. Lian, Z. Deng, M. H. Rümmeli, W. Yin, D. Zhang, S. Wang and Y. Peng, *Nat. Commun.*, 2019, **10**, 3782.
- 160 Y. Sun, B. Huang, Y. Li, Y. Xing, M. Luo, N. Li, Z. Xia, Y. Qin, D. Su, L. Wang and S. Guo, *Chem. Mater.*, 2019, **31**, 8136–8144.
- 161 Y. Mun, S. Lee, K. Kim, S. Kim, S. Lee, J. W. Han and J. Lee, *J. Am. Chem. Soc.*, 2019, **141**, 6254–6262.
- 162 X. Ao, W. Zhang, Z. Li, J.-G. Li, L. Soule, X. Huang, W.-H. Chiang, H. M. Chen, C. Wang, M. Liu and X. C. Zeng, *ACS Nano*, 2019, **13**, 11853–11862.
- 163 M. T. Darby, R. Réocreux, E. Charles, H. Sykes, A. Michaelides and M. Stamatakis, *ACS Catal.*, 2018, **8**, 5038–5050.
- 164 Y. Yao, S. Hu, W. Chen, Z.-Q. Huang, W. Wei, T. Yao, R. Liu, K. Zang, X. Wang, G. Wu, W. Yuan, T. Yuan, B. Zhu, W. Liu, Z. Li, D. He, Z. Xue, Y. Wang, X. Zheng, J. Dong, C.-R. Chang, Y. Chen, X. Hong, J. Luo, S. Wei, W.-X. Li, P. Strasser, Y. Wu and Y. Li, *Nat. Catal.*, 2019, **2**, 304–313.
- 165 B. Yu, H. Li, J. White, S. Donne, J. Yi, S. Xi, Y. Fu, G. Henkelman, H. Yu, Z. Chen and T. Ma, *Adv. Funct. Mater.*, 2020, **30**, 1905665.
- 166 M. Xiao, J. Zhu, G. Li, N. Li, S. Li, Z. P. Cano, L. Ma, P. Cui, P. Xu, G. Jiang, H. Jin, S. Wang, T. Wu, J. Lu, A. Yu, D. Su and Z. Chen, *Angew. Chem.*, 2019, **131**, 9742–9747.
- 167 S. Zhu, Q. Wang, X. Qin, M. Gu, R. Tao, B. P. Lee, L. Zhang, Y. Yao, T. Li and M. Shao, *Adv. Energy Mater.*, 2018, **8**, 1802238.
- 168 X. Zhang, Z. Sun, R. Jin, C. Zhu, C. Zhao, Y. Lin, Q. Guan, L. Cao, H. Wang, S. Li, H. Yu, X. Liu, L. Wang, S. Wei, W.-X. Li and J. Lu, *Nat. Commun.*, 2023, **14**, 530.
- 169 Q. Guan, C. Zhu, Y. Lin, E. I. Vovk, X. Zhou, Y. Yang, H. Yu, L. Cao, H. Wang, X. Zhang, X. Liu, M. Zhang, S. Wei, W.-X. Li and J. Lu, *Nat. Catal.*, 2021, **4**, 840–849.
- 170 S. Liu, Y. Li, X. Yu, S. Han, Y. Zhou, Y. Yang, H. Zhang, Z. Jiang, C. Zhu, W.-X. Li, C. Wöll, Y. Wang and W. Shen, *Nat. Commun.*, 2022, **13**, 4559.
- 171 X. Yuan, Y. Zhang, M. Cao, T. Zhou, X. Jiang, J. Chen, F. Lyu, Y. Xu, J. Luo, Q. Zhang and Y. Yin, *Nano Lett.*, 2019, **19**, 4752–4759.
- 172 A. Vojvodic, J. K. Nørskov and F. Abild-Pedersen, *Top. Catal.*, 2014, **57**, 25–32.
- 173 R. Hoffmann, *Rev. Mod. Phys.*, 1988, **60**, 601–628.
- 174 C. Hu, J. Hong, J. Huang, W. Chen, C. U. Segre, K. Suenaga, W. Zhao, F. Huang and J. Wang, *Energy Environ. Sci.*, 2020, **13**, 4249–4257.
- 175 H. Wang, J. Wang, Y. Pi, Q. Shao, Y. Tan and X. Huang, *Angew. Chem.*, 2019, **131**, 2338–2342.
- 176 L. Zhuang, Y. Jia, H. Liu, Z. Li, M. Li, L. Zhang, X. Wang, D. Yang, Z. Zhu and X. Yao, *Angew. Chem., Int. Ed.*, 2020, **59**, 14664–14670.
- 177 B.-A. Lu, L.-F. Shen, J. Liu, Q. Zhang, L.-Y. Wan, D. J. Morris, R.-X. Wang, Z.-Y. Zhou, G. Li, T. Sheng, L. Gu, P. Zhang, N. Tian and S.-G. Sun, *ACS Catal.*, 2021, **11**, 355–363.
- 178 J. Duan, S. Chen, C. A. Ortíz-Ledón, M. Jaroniec and S.-Z. Qiao, *Angew. Chem., Int. Ed.*, 2020, **59**, 8181–8186.
- 179 F. Lai, W. Zong, G. He, Y. Xu, H. Huang, B. Weng, D. Rao, J. A. Martens, J. Hofkens, I. P. Parkin and T. Liu, *Angew. Chem.*, 2020, **132**, 13422–13429.
- 180 Y. Li, B. Wei, M. Zhu, J. Chen, Q. Jiang, B. Yang, Y. Hou, L. Lei, Z. Li, R. Zhang and Y. Lu, *Adv. Mater.*, 2021, **33**, 2102212.
- 181 J. R. Kitchin, J. K. Nørskov, M. A. Bartea and J. G. Chen, *Phys. Rev. Lett.*, 2004, **93**, 156801.
- 182 H. Huang, H. Jia, Z. Liu, P. Gao, J. Zhao, Z. Luo, J. Yang and J. Zeng, *Angew. Chem.*, 2017, **129**, 3648–3652.
- 183 J. Yang, Z. Wang, C.-X. Huang, Y. Zhang, Q. Zhang, C. Chen, J. Du, X. Zhou, Y. Zhang, H. Zhou, L. Wang, X. Zheng, L. Gu, L.-M. Yang and Y. Wu, *Angew. Chem., Int. Ed.*, 2021, **60**, 22722–22728.
- 184 L. Zhai, B. T. W. Lo, Z.-L. Xu, J. Potter, J. Mo, X. Guo, C. C. Tang, S. C. Tsang and S. P. Lau, *ACS Energy Lett.*, 2020, **5**, 2483–2491.
- 185 Y. Zhou, R. Zhou, X. Zhu, N. Han, B. Song, T. Liu, G. Hu, Y. Li, J. Lu and Y. Li, *Adv. Mater.*, 2020, **32**, 2000992.

- 186 X.-L. Wang, L.-Z. Dong, M. Qiao, Y.-J. Tang, J. Liu, Y. Li, S.-L. Li, J.-X. Su and Y.-Q. Lan, *Angew. Chem., Int. Ed.*, 2018, **57**, 9660–9664.
- 187 B. Jiang, X.-G. Zhang, K. Jiang, D.-Y. Wu and W.-B. Cai, *J. Am. Chem. Soc.*, 2018, **140**, 2880–2889.
- 188 L. Ju, X. Tan, X. Mao, Y. Gu, S. Smith, A. Du, Z. Chen, C. Chen and L. Kou, *Nat. Commun.*, 2021, **12**, 5128.
- 189 F. Podjaski, D. Weber, S. Zhang, L. Diehl, R. Eger, V. Duppel, E. Alarcón-Lladó, G. Richter, F. Haase, A. Fontcuberta i Morral, C. Scheu and B. V. Lotsch, *Nat. Catal.*, 2020, **3**, 55–63.
- 190 R. P. Jansonius, L. M. Reid, C. N. Vircea and C. P. Berlinguet, *ACS Energy Lett.*, 2019, **4**, 980–986.
- 191 X. Wang, Y. Orikasa, Y. Takesue, H. Inoue, M. Nakamura, T. Minato, N. Hoshi and Y. Uchimoto, *J. Am. Chem. Soc.*, 2013, **135**, 5938–5941.
- 192 F. Ando, T. Gunji, T. Tanabe, I. Fukano, H. D. Abruña, J. Wu, T. Ohsaka and F. Matsumoto, *ACS Catal.*, 2021, **11**, 9317–9332.
- 193 S. Ye, F. Luo, Q. Zhang, P. Zhang, T. Xu, Q. Wang, D. He, L. Guo, Y. Zhang, C. He, X. Ouyang, M. Gu, J. Liu and X. Sun, *Energy Environ. Sci.*, 2019, **12**, 1000–1007.
- 194 H. Xin and S. Linic, *J. Chem. Phys.*, 2010, **132**, 221101.
- 195 I. Jana, S. Naskar, M. Das and D. Nandi, arXiv: Atomic and Molecular Clusters.
- 196 P.-P. Chen, J.-X. Liu and W.-X. Li, *ACS Catal.*, 2019, **9**, 8093–8103.
- 197 M. Yu and D. R. Trinkle, *J. Chem. Phys.*, 2011, **134**, 064111.
- 198 Q. Sun, M. Wang, Z. Li, A. Du and D. J. Searles, *Phys. Chem. Chem. Phys.*, 2016, 12695.
- 199 M. A. Dar and S. Krishnamurty, *ACS Omega*, 2019, **4**, 12687–12695.
- 200 M. Mavrikakis, B. Hammer and J. K. Nørskov, *Phys. Rev. Lett.*, 1998, **81**, 2819–2822.
- 201 M. Luo and S. Guo, *Nat. Rev. Mater.*, 2017, **2**, 1–13.
- 202 D. J. Shu, F. Liu and X. G. Gong, *Phys. Rev. B: Condens. Matter Mater. Phys.*, 2001, **64**, 245410.
- 203 R. G. S. Pala and F. Liu, *J. Chem. Phys.*, 2004, **120**, 7720–7724.
- 204 I. G. Shuttleworth, *Surf. Sci.*, 2017, **661**, 49–59.
- 205 F. Calle-Vallejo and A. S. Bandarenka, *ChemSusChem*, 2018, **11**, 1824–1828.
- 206 F. Liu, C. Wu, G. Yang and S. Yang, *J. Phys. Chem. C*, 2015, **119**, 15500–15505.
- 207 C. Wang, Y. Shi, D. Qin and Y. Xia, *Nanoscale Horiz.*, 2023, **8**, 1194–1204.
- 208 S. Gao, S. Hao, Z. Huang, Y. Yuan, S. Han, L. Lei, X. Zhang, R. Shahbazian-Yassar and J. Lu, *Nat. Commun.*, 2020, **11**, 2016.
- 209 G. Cao, J. Liang, Z. Guo, K. Yang, G. Wang, H. Wang, X. Wan, Z. Li, Y. Bai, Y. Zhang, J. Liu, Y. Feng, Z. Zheng, C. Lu, G. He, Z. Xiong, Z. Liu, S. Chen, Y. Guo, M. Zeng, J. Lin and L. Fu, *Nature*, 2023, **619**, 73–77.
- 210 Y. Liao, Y. Li, R. Zhao, J. Zhang, L. Zhao, L. Ji, Z. Zhang, X. Liu, G. Qin and X. Zhang, *Natl. Sci. Rev.*, 2022, **9**, nwac041.
- 211 R. K. Pittkowski, C. M. Clausen, Q. Chen, D. Stoian, W. van Beek, J. Bucher, R. L. Welten, N. Schlegel, J. K. Mathiesen, T. M. Nielsen, J. Du, A. W. Rosenkranz, E. D. Bøjesen, J. Rossmeisl, K. M. Ø. Jensen and M. Arenz, *EES Catal.*, 2023, **1**, 950–960.
- 212 G. Feng, F. Ning, J. Song, H. Shang, K. Zhang, Z. Ding, P. Gao, W. Chu and D. Xia, *J. Am. Chem. Soc.*, 2021, **143**, 17117–17127.
- 213 D. Wu, K. Kusada, Y. Nanba, M. Koyama, T. Yamamoto, T. Toriyama, S. Matsumura, O. Seo, I. Gueye, J. Kim, L. S. R. Kumara, O. Sakata, S. Kawaguchi, Y. Kubota and H. Kitagawa, *J. Am. Chem. Soc.*, 2022, **144**, 3365–3369.
- 214 L. Xiao, Z. Wang and J. Guan, *Chem. Sci.*, 2023, **14**, 12850–12868.
- 215 S. Niu, Z. Yang, F. Qi, Y. Han, Z. Shi, Q. Qiu, X. Han, Y. Wang and X. Du, *Adv. Funct. Mater.*, 2022, **32**, 2203787.
- 216 Y. Leng, Z. Zhang, H. Chen, S. Du, J. Liu, S. Nie, Y. Dong, P. Zhang and S. Dai, *Chem. Commun.*, 2021, **57**, 3676–3679.
- 217 S. Dong, H. Zhou, X. Hu, J. Zhang, Y. Li, W. Shang, Z. Liu, L. Wan and H. Zhao, *Int. J. Hydrogen Energy*, 2023, **48**, 18233–18244.
- 218 R. Yu, Y. Liu, X. Sun, G. He, H. Dong, S. Deng, J. Li and Y. Chu, *Sci. China Mater.*, 2023, **66**, 3582–3591.